Pullback Flow Matching on Data Manifolds

Friso de Kruiff [1 2 3] **Erik Bekkers** [3] **Ozan Öktem** [1] **Carola-Bibiane Schönlieb** [4] **Willem Diepeveen** [5]

Abstract

We propose Pullback Flow Matching (PFM), a novel framework for generative modeling on data manifolds. Unlike existing methods that assume or learn restrictive closed-form manifold mappings for training Riemannian Flow Matching (RFM) models, PFM leverages pullback geometry and isometric learning to preserve the underlying manifold's geometry while enabling efficient generation and precise interpolation in latent space. This approach not only facilitates closed-form mappings on the data manifold but also allows for designable latent spaces, using assumed metrics on both data and latent manifolds. By enhancing isometric learning through Neural ODEs and proposing a scalable training objective, we achieve a latent space more suitable for interpolation, leading to improved manifold learning and generative performance. We demonstrate PFM's effectiveness through applications in synthetic data, protein dynamics and protein sequence data, generating novel proteins with specific properties. This method shows strong potential for drug discovery and materials science, where generating novel samples with specific properties is of great interest.

1. Introduction

Since the rise of machine learning in the scientific domain, researchers have focused on developing larger models trained on increasingly massive datasets, as in weather forecasting (Bodnar et al., 2024) and protein structure prediction (Hayes et al., 2024). However, relying on such scaling laws is not feasible in many scientific fields where data is limited

[1]Department of Mathematics, KTH Royal Institute of Technology [2]Department of Applied Mathematics, Delft University of Technology [3]AMLab, University of Amsterdam [4]DAMTP, University of Cambridge [5]Department of Mathematics, University of California, Los Angeles. Correspondence to: Friso de Kruiff <f.c.dekruiff@uva.nl>.

Proceedings of the Workshop on Generative AI for Biology at the 42nd International Conference on Machine Learning, Vancouver, Canada. PMLR 267, 2025. Copyright 2025 by the author(s).

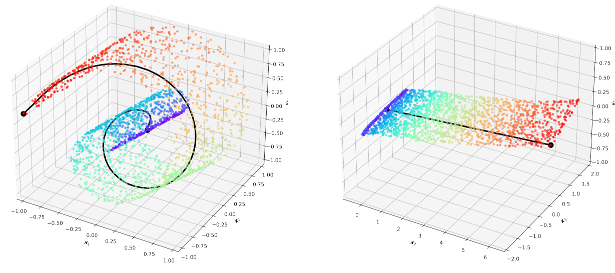

Data manifold ($\mathcal{D}$) *Latent manifold* ($\mathcal{M}$)

Figure 1: Isometric learning for the rotated Swiss roll in 3D. The learned geodesic path (in black) on the data manifold $\mathcal{D} \subset \mathbb{R}^3$ correspond to the shortest paths on the latent manifold $\mathcal{M} = \mathbb{R}^3$.

and precise modeling of physical phenomena is crucial. In such cases, incorporating prior knowledge about the geometry of the data as an inductive bias enables models to make accurate interpolations between data points, which is essential for reliable predictions and realistic representations of complex systems.

Current methods, however, lack the mathematical foundations to accurately interpolate in latent space (Arvanitidis et al., 2017) and do not capture the underlying geometric structure of the data (Wessels et al., 2024). Our goal is to develop mappings that enable precise interpolation in latent space, leveraging geometry as an inductive bias to facilitate efficient and accurate generation on data manifolds, thereby advancing the ability to model complex physical phenomena with limited data.

We consider modeling the data under the manifold hypothesis, which states that high-dimensional data lies on a lower dimensional manifold. This has been applied successfully to various scientific tasks (Vanderplas & Connolly, 2009; Dsilva et al., 2016; Noé & Clementi, 2017). Modeling the data in its intrinsic dimension allows for efficient analysis (Diepeveen et al., 2024) and generation (Rombach et al., 2022). Furthermore, accurately capturing the geometry of the data manifold in the learning problem has shown to improve several down-stream tasks such as clustering (Ghojogh et al., 2022), classification (Kaya & Bilge, 2019; Hauberg et al., 2012) and generation (Arvanitidis et al., 2020; Sun et al., 2024).

One way to achieve a latent manifold that supports interpolation is to have a structured Riemannian geometry, such as the one from *pullback geometry*, which provides closed-form manifold mappings (Diepeveen et al., 2024). This requires constructing an invertible and differentiable mapping—*diffeomorphism*—between the data manifold and the latent manifold. Interpolation on manifolds is then performed through geodesics, shortest paths, and thus to achieve our goal we require geodesics on the data manifold to match geodesics on the latent manifold. This motivates our consideration of *isometries*, that is, metric-preserving diffeomorphisms φ. These mappings preserve the distances of points on the data manifold on the latent manifold, and thereby ensure proper interpolation.

Related-Work. In the literature, low-dimensional generation and generation on manifolds have typically been addressed as separate problems. Low-dimensional approaches, such as latent diffusion (Rombach et al., 2022) or latent flow-matching (Dao et al., 2023), often overlook the geometric structure of the data, leading to inaccuracies in tasks requiring a faithful representation of the underlying manifold. Conversely, manifold generation methods either assume geodesics on the data manifold for simulation-free training (Chen & Lipman, 2024)—an approach inapplicable when closed-form mappings are unavailable—or attempt to learn a metric that forces the generative trajectories to have data support (Kapusniak et al., 2024).

Using a pullback framework presents challenges, such as task-specific learning problems that limit generality and prevent the learning of isometries across broader data manifolds (Cuzzolin, 2008; Gruffaz et al., 2021; Lebanon, 2006). Geometrically regularized latent space methods, like (Lee et al., 2022) and (Duque et al., 2022), work in practice but lack solid mathematical grounding in isometries, particularly guaranteeing diffeomorphism in architectural design. (Diepeveen, 2024) addresses isometry challenges with a more general mathematical framework, but its learning objective's expressivity and computational feasibility limit its application to high-dimensional real-world datasets.

Our approach bridges these gaps by modeling data on a lower-dimensional latent manifold with known geometry through diffeomorphisms parameterized and trained in a scalable and expressive way. By doing so we preserve the intrinsic properties of the data manifold and enable accurate and efficient generation through simulation-free training.

Contributions. We propose PFM, a novel framework for latent manifold learning and generation through isometries. This method respects the geometry of the data manifold, even when closed-form manifold mappings are not available. Second, learning can be performed in the intrinsic dimension of the data manifold resulting in efficient and effective learning of the generative model with fewer parameters. We leverage pullback geometry to define a new metric on the entire ambient space, $\mathbb{R}^d$, by learning an isometry φ that preserves the geometric structure of the data manifold $\mathcal{D}$ on the latent manifold $\mathcal{M}$. We use the corresponding metric of the assumed latent manifold $\mathcal{M}$ to perform RFM. Our contributions are:

1. We introduce PFM, a novel framework that enables accurate and efficient data generation on manifolds. PFM leverages the pullback geometry to preserve the underlying geometric structure of the data manifold within the latent space, facilitating precise interpolation and generation.
2. We improve the parameterization of diffeomorphisms, used to learn isometries, in both expressiveness and training efficiency through neural ordinary differential equations (Neural ODEs).
3. We introduce a scalable and stable isometric learning objective. This objective relies solely on a distance measure on the data manifold, simplifying the training process compared to (Diepeveen, 2024) while maintaining geometric fidelity.
4. We demonstrate our methods' effectiveness through experiments on synthetic data, high-dimensional molecular dynamics data, and experimental peptide sequences. Our framework utilizes *designable latent spaces* to generate novel proteins with specific properties closely matching reference samples. This directed generation showcases the significant applicability of isometric learning and PFM in accurate physical modeling and interpolation, advancing generative modeling techniques in drug discovery and materials science.

2. Notation

We give a brief summary of the notation used in the paper, and give a more extensive background on Riemannian and pullback geometry in Appendix A.

A *manifold* $\mathcal{M}$ is a topological space that locally resembles Euclidean space. A d-dimensional manifold $\mathcal{M}$ around a point $\boldsymbol{p} \in \mathcal{M}$ is described by a *chart* $\psi : U \to \mathbb{R}^d$, where $U \subseteq \mathcal{M}$ is a neighborhood of $\boldsymbol{p}$. The chart provides a local coordinate system for the manifold. The *tangent space* at a point $\boldsymbol{p} \in \mathcal{M}$, denoted $\mathcal{T}_{\boldsymbol{p}}\mathcal{M}$, is the vector space of all tangent vectors at that point.

A smooth manifold $\mathcal{M}$ equipped with a *Riemannian metric* is called a *Riemannian manifold* and is denoted by $(\mathcal{M}, (\cdot,\cdot)^{\mathcal{M}})$. The Riemannian metric $(\cdot,\cdot)^{\mathcal{M}}$ is a smoothly varying inner product defined on the tangent spaces $\mathcal{T}_{\boldsymbol{p}}\mathcal{M}$ for all points $\boldsymbol{p} \in \mathcal{M}$, and it defines lengths and angles on the manifold. A *geodesic*, $\gamma_{\boldsymbol{p},\boldsymbol{q}}(t)$ is the shortest path between two points $\boldsymbol{p}, \boldsymbol{q} \in \mathcal{M}$, generalizing the notion of a straight line in Euclidean space.

The *exponential map* $\exp_{\boldsymbol{p}} : \mathcal{T}_{\boldsymbol{p}}\mathcal{M} \to \mathcal{M}$ maps a tangent vector $\Xi_{\boldsymbol{p}}$ to a point on the manifold by following the geodesic in the direction of $\Xi_{\boldsymbol{p}}$ starting from $\boldsymbol{p}$. The inverse of the exponential map is the *logarithmic map*, denoted by $\log_{\boldsymbol{p}} : \mathcal{M} \to \mathcal{T}_{\boldsymbol{p}}\mathcal{M}$, which returns the tangent vector corresponding to a given point on the manifold.

In this work, we consider a d-dimensional Riemannian manifold $\left(\mathcal{M}, (\cdot,\cdot)^{\mathcal{M}}\right)$, and a smooth diffeomorphism $\varphi : \mathbb{R}^d \to \mathcal{M}$, such that $\varphi\left(\mathbb{R}^d\right) \subseteq \mathcal{M}$ is geodesically convex, meaning that any pair of points within this subset are connected by a unique geodesic.

This mapping allows us to pullback the geometric structure of $\mathcal{M}$ to $\mathbb{R}^d$ by defining the *pullback metric* on $\mathbb{R}^d$. Specifically, for tangent vectors $\Xi_{\boldsymbol{p}}, \Phi_{\boldsymbol{p}} \in \mathcal{T}_{\boldsymbol{p}}\mathbb{R}^d$, the pullback metric is defined as

$$(\Xi_{\boldsymbol{p}}, \Phi_{\boldsymbol{p}})^{\varphi} := \left(\varphi_*[\Xi_{\boldsymbol{p}}], \varphi_*[\Phi_{\boldsymbol{p}}]\right)^{\mathcal{M}}_{\varphi(\boldsymbol{p})}, \tag{1}$$

where φ_* is the pushforward of tangent vectors under φ. Through this construction, various geometric objects in $\mathcal{M}$, such as distances and geodesics, can be expressed in terms of their counterparts in $\mathbb{R}^d$ with respect to the pullback metric.

The distance function $d^{\varphi}_{\mathbb{R}^d} : \mathbb{R}^d \times \mathbb{R}^d \to \mathbb{R}$ on $\mathbb{R}^d$ with the pullback metric is given by,

$$d^{\varphi}_{\mathbb{R}^d}(\boldsymbol{x}_i, \boldsymbol{x}_j) = d_{\mathcal{M}}\left(\varphi(\boldsymbol{x}_i), \varphi(\boldsymbol{x}_j)\right), \tag{2}$$

where $d_{\mathcal{M}}$ denotes the Riemannian distance on $\mathcal{M}$. The length-minimizing geodesic connecting $\boldsymbol{x}_i$ and $\boldsymbol{x}_j$ in $\mathbb{R}^d$ with respect to the pullback metric $\gamma^{\varphi}_{\boldsymbol{x}_i,\boldsymbol{x}_j} : [0,1] \to \mathbb{R}^d$ is given by,

$$\gamma^{\varphi}_{\boldsymbol{x}_i,\boldsymbol{x}_j}(t) = \varphi^{-1}\left(\gamma^{\mathcal{M}}_{\varphi(\boldsymbol{x}_i),\varphi(\boldsymbol{x}_j)}(t)\right), \tag{3}$$

here $\gamma^{\mathcal{M}}$ denotes the geodesic in $\mathcal{M}$ connecting $\varphi(\boldsymbol{x}_i)$ and $\varphi(\boldsymbol{x}_j)$. This enables computation of geodesics and distances in $\mathbb{R}^d$ using the geometry of $\mathcal{M}$, as stated in Prop. 2.1 of (Diepeveen, 2024).

In this paper we will assume the standard Euclidean metric $(\cdot,\cdot)_2$ and a Euclidean latent manifold $\mathcal{M} = \mathbb{R}^d$. Hence, the pullback metric will be defined as

$$(\Xi_{\boldsymbol{p}}, \Phi_{\boldsymbol{p}})^{\varphi} := \left(\varphi_*[\Xi_{\boldsymbol{p}}], \varphi_*[\Phi_{\boldsymbol{p}}]\right)^{\mathbb{R}^d}_{\varphi(\boldsymbol{p})}. \tag{4}$$

We will calculate distances on the latent manifold $\mathcal{M} = \mathbb{R}^d$ through,

$$d^{\varphi}_{\mathbb{R}^d}(\boldsymbol{x}_i, \boldsymbol{x}_j) = \|\varphi(\boldsymbol{x}_i) - \varphi(\boldsymbol{x}_j)\|_2, \tag{5}$$

and the geodesic calculation will boil down to

$$\gamma^{\varphi}_{\boldsymbol{x}_i,\boldsymbol{x}_j}(t) = \varphi^{-1}\left(\varphi(\boldsymbol{x}_i)(1-t) + t\varphi(\boldsymbol{x}_j)\right). \tag{6}$$

An example of a pullback geodesic $\gamma^{\varphi}_{\boldsymbol{x}_i,\boldsymbol{x}_j}(t)$ on the data manifold based on a geodesic on a latent Euclidean manifold can be viewed in Figure 1.

3. Pullback Flow Matching

We propose *Pullback Flow Matching (PFM)*, a novel framework for generative modeling on data manifolds using *pullback geometry*. Our goal is to transform samples from a simple distribution $\boldsymbol{x}_0 \sim p$ on the data manifold $\mathcal{D}$ into a complex target distribution $\boldsymbol{x}_1 \sim q$, also on $\mathcal{D}$. Ideally, we would perform this transformation using *Riemannian Flow Matching (RFM)*, see Appendix A for a summary, on $\left(\mathcal{D}, (\cdot,\cdot)^{\mathcal{D}}\right)$ by optimizing the objective from (Chen & Lipman, 2024),

$$\mathcal{L}_{RFM}(\boldsymbol{\eta}) = \mathbb{E}_{t,q(\boldsymbol{x}_1),p(\boldsymbol{x}_0)}\left(\left\|v_t(\gamma^{\mathcal{D}}_{\boldsymbol{x}_1,\boldsymbol{x}_0}(t);\boldsymbol{\eta}) - \dot{\gamma}^{\mathcal{D}}_{\boldsymbol{x}_1,\boldsymbol{x}_0}(t)\right\|^{\mathcal{D}}_{\gamma^{\mathcal{D}}_{\boldsymbol{x}_1,\boldsymbol{x}_0}(t)}\right)^2, \tag{7}$$

where $\boldsymbol{\eta}$ represents the learnable parameters of the parameterized vector field $v_t(\boldsymbol{x};\boldsymbol{\eta})$. Solving this objective on data manifolds becomes intractable as the training of RFM is no longer simulation-free (Chen & Lipman, 2024). Existing methods address this challenge by employing restrictive and computationally intensive manifold mappings (Kapusniak et al., 2024). We overcome this limitation by defining a new metric on the ambient space $\mathbb{R}^d$ using the *pullback metric* (Diepeveen, 2024) and assume a learned *isometry* $\varphi_{\boldsymbol{\theta}}$ that approximates geodesics $\gamma^{\varphi_{\boldsymbol{\theta}}}$ on $\left(\mathbb{R}^d, (\cdot,\cdot)^{\varphi_{\boldsymbol{\theta}}}\right)$ to those $\gamma^{\mathcal{D}}$ on $\left(\mathcal{D}, (\cdot,\cdot)^{\mathcal{D}}\right)$. Rewriting the RFM objective under the pullback framework yields the objective,

$$\mathcal{L}_{PFM}(\boldsymbol{\eta}) = \mathbb{E}_{t,q(\boldsymbol{x}_1),p(\boldsymbol{x}_0)}\left(\left\|v_t\left(\gamma^{\varphi_{\boldsymbol{\theta}}}_{\boldsymbol{x}_1,\boldsymbol{x}_0}(t);\boldsymbol{\eta}\right) - \dot{\gamma}^{\varphi_{\boldsymbol{\theta}}}_{\boldsymbol{x}_1,\boldsymbol{x}_0}(t)\right\|^{\varphi_{\boldsymbol{\theta}}}_{\gamma^{\varphi_{\boldsymbol{\theta}}}_{\boldsymbol{x}_1,\boldsymbol{x}_0}(t)}\right)^2, \tag{8}$$

By applying Equation 3, we reformulate the PFM objective in terms of manifold mappings on $\mathcal{M}$,

$$\mathcal{L}_{PFM}(\boldsymbol{\eta}) = \mathbb{E}_{t,q(\boldsymbol{x}_1),p(\boldsymbol{x}_0)}\left(\left\|v_t\left(\gamma^{\mathcal{M}}_{\varphi_{\boldsymbol{\theta}}(\boldsymbol{x}_1),\varphi_{\boldsymbol{\theta}}(\boldsymbol{x}_0)}(t);\boldsymbol{\eta}\right) - \dot{\gamma}^{\mathcal{M}}_{\varphi_{\boldsymbol{\theta}}(\boldsymbol{x}_1),\varphi_{\boldsymbol{\theta}}(\boldsymbol{x}_0)}(t)\right\|^{\mathcal{M}}_{\gamma^{\mathcal{M}}_{\varphi_{\boldsymbol{\theta}}(\boldsymbol{x}_1),\varphi_{\boldsymbol{\theta}}(\boldsymbol{x}_0)}(t)}\right)^2, \tag{9}$$

Assuming a latent manifold $\mathcal{M}$ with closed-form mappings enables simulation-free training on data manifolds. For efficiency, we model the d-dimensional latent manifold as a product manifold, $\mathcal{M} = \mathcal{M}_{d'} \times \mathbb{R}^{d-d'}$. By encoding samples close to the submanifold $\mathcal{M}_{d'} \subset \mathcal{M}$, isometric learning ensures geodesics $\mathcal{M}_{d'}$ closely match geodesics on

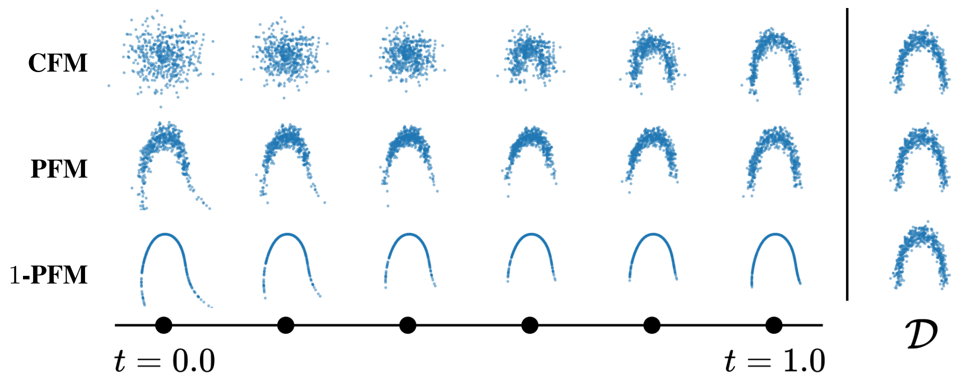

Figure 2: Trajectories of continous normalizing flows (CNF) (left) trained with Conditional Flow Matching (CFM), PFM and 1-PFM objectives on the ARCH dataset compared to the data manifold $\mathcal{D}$ (right). At $t = 0$ the trajectory starts with a standard normal distribution in the data space for CFM and latent submanifold for (1-)PFM mapped back to the data space.

$\mathcal{M}$. As a result, we formulate the d'-PFM objective,

$$\begin{aligned}&\mathcal{L}_{d'-PFM}(\boldsymbol{\eta}) = \\ &\mathbb{E}_{t,q(\boldsymbol{x}_1),p(\boldsymbol{x}_0)}\left(\left\| v_t\left(\gamma^{\mathcal{M}_{d'}}_{\varphi_{\boldsymbol{\theta}}(\boldsymbol{x}_1),\varphi_{\boldsymbol{\theta}}(\boldsymbol{x}_0)}(t);\boldsymbol{\eta}\right) - \right.\right. \\ &\left.\left. \dot{\gamma}^{\mathcal{M}_{d'}}_{\varphi_{\boldsymbol{\theta}}(\boldsymbol{x}_1),\varphi_{\boldsymbol{\theta}}(\boldsymbol{x}_0)}(t)^{\mathcal{M}_{d'}}_{\gamma^{\mathcal{M}_{d'}}_{\varphi_{\boldsymbol{\theta}}(\boldsymbol{x}_1),\varphi_{\boldsymbol{\theta}}(\boldsymbol{x}_0)}(t)}\right)^2,\end{aligned} \tag{10}$$

The d'-PFM objective offers two key benefits. Defining the objective on the submanifold $\mathcal{M}_{d'}$ results in computational speed-ups during training. Second, the known geometry on the submanifold simplifies the training dynamics of the vector field $v_t(\cdot;\boldsymbol{\eta})$, requiring fewer parameters $\boldsymbol{\eta}$ to learn the sampling trajectories of the data manifold, see Table 3.

4. Learning Isometries

The motivation for learning isometries $\varphi_{\boldsymbol{\theta}}$—metric-preserving diffeomorphisms—is to obtain a latent (sub)manifold that supports interpolation with closed-form geometric mappings, facilitating efficient simulation-free training of PFM. Our approach aligns with the isometry learning framework introduced by Diepeveen (Diepeveen, 2024), but differs in two crucial ways. First, we propose a more expressive parameterization of learnable diffeomorphisms via neural ordinary differential equations (NODEs). Second, we introduce a novel training objective that enables scalable isometric learning on data manifolds.

4.1. Parameterizing Diffeomorphisms

We parameterize diffeomorphisms, invertible and differentiable functions between two manifolds, specifically $\varphi : \mathbb{R}^d \to \mathcal{M}$. In practice, we construct a product manifold, $\mathcal{M} = \mathcal{M}_{d'} \times \mathbb{R}^{d-d'}$ and the diffeomorphism φ as,

$$\varphi := [\psi^{-1}, \boldsymbol{I}_{d-d'}] \circ \phi \circ T_{\boldsymbol{\mu}}, \tag{11}$$

where $\psi : U \to \mathbb{R}^{d'}$ a chart on a geodesically convex subset $U \subset \mathcal{M}_{d'}$ of the d'-dimensional latent submanifold $\left(\mathcal{M}_{d'}, (\cdot,\cdot)_{\mathcal{M}_{d'}}\right)$. See Appendix B for a list of manifolds with closed-form expressions for the exponential and logarithmic maps, and how these maps can be used to construct a chart ψ. Furthermore, $\phi : \mathbb{R}^d \to \mathbb{R}^d$ is a diffeomorphism and $T_{\boldsymbol{\mu}}(\boldsymbol{x}) = \boldsymbol{x} - \boldsymbol{\mu}$, with $\boldsymbol{\mu}$ the average of the datapoints. We choose this construction because the manifold hypothesis translates to assuming the data manifold is homeomorphic to $\mathcal{M}_{d'}$. In such case, the rest of the latent manifold should be mapped close to zero, e.g. $\varphi(\boldsymbol{x}_i)$ is close to $\mathcal{M}_{d'} \times \mathbf{0}^{d-d'}$ in terms of the metric on $\mathcal{M}$.

We generate the diffeomorphism ϕ by learning a Neural ODE (Chen et al., 2018). The advantage of this approach is threefold, *i)* this parameterization of diffeomorphisms is more expressive and efficient to train compared to Invertible Residual Networks (Behrmann et al., 2019) as chosen by (Diepeveen, 2024), *ii)* based on some mild technical assumptions a Neural ODE can be proven to generate proper diffeomorphisms, see Appendix C for the proof, and *iii)* numerically the accuracy and invertibility of the generated flow can be controlled through smaller step-sizes and higher-order solvers.

To define the diffeomorphism $\phi_{\boldsymbol{\theta}} : \mathbb{R}^d \to \mathbb{R}^d$, we start with the Neural ODE governing the flow:

$$\frac{d\boldsymbol{z}(t)}{dt} = f(\boldsymbol{z}(t);\boldsymbol{\theta}), \tag{12}$$

where $f : \mathbb{R}^d \to \mathbb{R}^d$ is a vector field parameterized by a multilayer perceptron (MLP) with Swish activation functions and a sine-cosine time embedding and $\boldsymbol{\theta}$ denotes the parameters of the MLP. Given an initial condition $\boldsymbol{z}(0) = \boldsymbol{x}$, the solution to this Neural ODE is:

$$\phi_{\boldsymbol{\theta}}(\boldsymbol{x}) := \boldsymbol{x} + \int_0^1 f(\boldsymbol{z}(t);\boldsymbol{\theta})\, dt. \tag{13}$$

To obtain the inverse $\phi_{\boldsymbol{\theta}}^{-1}$ one has to integrate the differential equation backwards in time with initial condition $\boldsymbol{z}(1)$. To solve the Neural ODE we implemented a Runge-Kutta solver in `JAX`, see Appendix F for further architectural and training related details.

4.2. Learning Objective

The primary objectives of learning isometries are *i)* to map the data manifold $\left(\mathcal{D}, (\cdot,\cdot)^{\mathcal{D}}\right)$ into a low-dimensional geodesic subspace of $\left(\mathcal{M}, (\cdot,\cdot)^{\mathcal{M}}\right)$, specifically $\mathcal{M}_{d'} \subset \mathcal{M}$, and *ii)* to preserve local isometry, as motivated by Proposition 2.1 and Theorems 3.4, 3.6, and 3.8 from (Diepeveen, 2024).

We improve the training objective of Diepeveen (2024) by incorporating **graph matching loss** for isometric learning, enforcing global isometry between data and latent manifolds (Zhu et al., 2014), ensuring each sample remains equally isometric to all others. Additionally, we use **global isometry loss** and **submanifold loss** to map the data manifold $\mathcal{D}$ onto the lower-dimensional geodesic subspace $\mathcal{M}_{d'}$.

The original objective enforces local isometry—preserving geodesic distances in small neighborhoods—via the pullback metric's Riemannian tensor $(\cdot,\cdot)^{\varphi}$. However, this is computationally intractable and poorly scalable. We address this by using the regularization in **stability regularization** from (Finlay et al., 2020), which more efficiently enforces local isometry, leading to a scalable objective,

$$\mathcal{L}(\boldsymbol{\theta}) = \alpha_1 \frac{1}{n^2}\sum_{i=1}^{n}\sum_{j=1}^{n} \|d_{\mathbb{R}^d}^{\varphi_{\boldsymbol{\theta}}}(\boldsymbol{x}_i,\boldsymbol{x}_j) - d_{i,j}\|^2 \qquad \text{(global isometry loss)}$$

$$+ \alpha_2 \frac{1}{n}\sum_{i=1}^{n}\sum_{j\neq i} \|(\boldsymbol{d}_{\mathbb{R}^d}^{\varphi_{\boldsymbol{\theta}}}(\boldsymbol{x}_i,\boldsymbol{x}_\cdot) - \boldsymbol{d}_{\mathbb{R}^d}^{\varphi_{\boldsymbol{\theta}}}(\boldsymbol{x}_j,\boldsymbol{x}_\cdot)) - (\boldsymbol{d}_{i,\cdot} - \boldsymbol{d}_{j,\cdot})\|^2 \qquad \text{(graph matching loss)}$$

$$+ \alpha_3 \frac{1}{n}\sum_{i=1}^{n} \left\| \begin{bmatrix} \mathbf{0}_{d'} & \emptyset \\ \emptyset & \boldsymbol{I}_{d-d'} \end{bmatrix} (\phi_{\boldsymbol{\theta}} \circ T_{\boldsymbol{\mu}})(\boldsymbol{x}_i) \right\|_1 \qquad \text{(submanifold loss)}$$

$$+ \alpha_4 \frac{1}{n}\sum_{i=1}^{n} \int_0^1 \|\boldsymbol{\varepsilon}^T \nabla f_{\boldsymbol{\theta}}(\boldsymbol{z}_i(t))\|^2 \, dt. \qquad \text{(stability regularization)}$$

Here, $\boldsymbol{\varepsilon} \sim \mathcal{N}(\mathbf{0}, \boldsymbol{I})$ and $\boldsymbol{d}_{\mathbb{R}^d}^{\varphi_{\boldsymbol{\theta}}}(\boldsymbol{x}_i,\boldsymbol{x}_\cdot)$ and $\boldsymbol{d}_{i,\cdot}$ denote the columns of the distance matrices induced by $(\cdot,\cdot)^{\varphi}$ and $(\cdot,\cdot)^{\mathcal{D}}$. The benefit of this formulation is that it only requires approximating geodesic distances $d_{i,j}$ on the data manifold $\mathcal{D}$, without needing to calculate or differentiate the metric tensor. In section 5, we demonstrate the effectiveness of the graph matching loss and stability regularization through an ablation study on synthetic and high-dimensional protein dynamics trajectories. We do not include an ablation of the global isometry loss and submanifold losses, as these have been thoroughly examined in (Diepeveen, 2024), and our experiments showed consistent results with those previously reported.

5. Experiments

The goal of this paper is to learn interpolatable latent (sub)manifolds for generation on data manifolds. We achieve this through isometric learning in the framework of pullback geometry. In this section we validate our methods on synthetic, simulated and experimental datasets, for full descriptions see Appendix E. For details on the training procedure and hyperparameter settings we refer the reader to Appendix F.

We begin our experiments with an ablation study of **graph matching loss** and **stability regularization**, demonstrating the benefits of including both terms for learning isometries. Second, we compare (latent) interpolation methods with interpolation on the latent manifold $\mathcal{M}$, $(\cdot,\cdot)^{\mathcal{M}}$-interpolation, and on the latent submanifold $\mathcal{M}_{d'}$, $(\cdot,\cdot)^{\mathcal{M}_{d'}}$-interpolation. We demonstrate that we can accurately interpolate on the data manifold by interpolating on the latent (sub)manifold [1]. Third, we validate PFM as a generative model on data manifolds and discuss how sample generation is improved by generating on the submanifold $\mathcal{M}_{d'}$. Finally, we inspect the designability of the latent manifold through the choice of metric $(\cdot,\cdot)^{\mathcal{D}}$ in the task of small protein design.

5.1. Ablation Study

The goal of the ablation study is to evaluate the effectiveness of the reformulated objective function for learning isometries. To this end, we perform an ablation study for both the **graph matching loss** and **stability regularization** on a synthetic ARCH dataset ($n = 500$, $d = 2$) in the spirit of (Tong et al., 2020) and a coarse-grained protein dynamics datasets of intestinal fatty acid binding protein (I-FABP) ($n = 500$, $d = 131 \times 3$). We report three metrics on the validation set of 20 % of the data, invertibility $\varepsilon_{inv} = \frac{1}{n}\sum_{i=1}^{n} \|\boldsymbol{x}_i - \varphi_{\boldsymbol{\theta}}^{-1}(\varphi_{\boldsymbol{\theta}}(\boldsymbol{x}_i))\|^2$, low-dimensionality $\varepsilon_{ld} = \frac{1}{n}\sum_{i=1}^{n} \left\| \begin{bmatrix} \mathbf{0}_{d'} & \emptyset \\ \emptyset & \boldsymbol{I}_{d-d'} \end{bmatrix} \phi_{\boldsymbol{\theta}}(\boldsymbol{x}_i) \right\|_1^2$ and isometry $\varepsilon_{iso} = \frac{1}{n^2}\sum_{i=1}^{n}\sum_{j=1}^{n} \|d_{i,j} - d_{\mathcal{M}}(\varphi(\boldsymbol{x}_i), \varphi(\boldsymbol{x}_j))\|^2$.

Result. Table 1 demonstrates that incorporating both the graph matching loss and stability regularization improves the invertibility and isometry metrics across both datasets, with the combined approach yielding both a low ε_{inv} and ε_{iso} values, indicating enhanced model performance in pre-

[1] In these experiments we do not report interpolation through the Riemannian Auto-Encoder (RAE) by (Diepeveen, 2024) due to the intractability of the training objective for the higher-dimensional datasets.

Table 1: Ablation study of isometric learning for ARCH dataset and I-FABP protein dynamics datasets for **graph matching loss** (GM) and **stability regularization** (Stability). In both cases we choose $\mathcal{M}_{d'} = \mathbb{R}$. We report the means for invertibility (↓), low-dimensionality (↓) and isometry (↓) with standard devations denoted by $\pm$. The distance $(\cdot,\cdot)^{\mathcal{D}}$ we assume on the data manifold $\mathcal{D}$ is a locally Euclidean distance based on Isomap (Tenenbaum et al., 2000).

Data	Metric	None	GM	Stability	Both
ARCH	Invertibility	$7.637 \cdot 10^{-1}$ $\pm 9.872 \cdot 10^{-1}$	$3.585 \cdot 10^{-2}$ $\pm 1.939 \cdot 10^{-2}$	$\mathbf{8.198 \cdot 10^{-5}}$ $\pm 1.061 \cdot 10^{-5}$	$1.011 \cdot 10^{-4}$ $\pm 6.069 \cdot 10^{-5}$
	Low-Dimensionality	$6.520 \cdot 10^{-4}$ $\pm 9.521 \cdot 10^{-5}$	$\mathbf{4.531 \cdot 10^{-4}}$ $\pm 3.341 \cdot 10^{-5}$	$1.407 \cdot 10^{-2}$ $\pm 8.414 \cdot 10^{-4}$	$1.373 \cdot 10^{-2}$ $\pm 6.768 \cdot 10^{-4}$
	Isometry	$2.334 \cdot 10^{-3}$ $\pm 1.466 \cdot 10^{-4}$	$\mathbf{1.464 \cdot 10^{-3}}$ $\pm 1.221 \cdot 10^{-4}$	$2.018 \cdot 10^{-3}$ $\pm 5.791 \cdot 10^{-5}$	$1.544 \cdot 10^{-3}$ $\pm 2.025 \cdot 10^{-4}$
I-FABP	Invertibility	$2.995 \cdot 10^{-5}$ $\pm 8.945 \cdot 10^{-6}$	$2.891 \cdot 10^{-5}$ $\pm 4.968 \cdot 10^{-6}$	$2.973 \cdot 10^{-5}$ $\pm 7.560 \cdot 10^{-6}$	$\mathbf{2.809 \cdot 10^{-5}}$ $\pm 8.982 \cdot 10^{-6}$
	Low-Dimensionality	$\mathbf{1.378 \cdot 10^{-1}}$ $\pm 1.952 \cdot 10^{-4}$	$1.379 \cdot 10^{-1}$ $\pm 1.424 \cdot 10^{-4}$	$1.379 \cdot 10^{-1}$ $\pm 1.788 \cdot 10^{-4}$	$\mathbf{1.378 \cdot 10^{-1}}$ $\pm 1.981 \cdot 10^{-4}$
	Isometry	$2.889 \cdot 10^{-3}$ $\pm 1.384 \cdot 10^{-4}$	$2.898 \cdot 10^{-3}$ $\pm 1.667 \cdot 10^{-4}$	$2.919 \cdot 10^{-3}$ $\pm 1.571 \cdot 10^{-4}$	$\mathbf{2.887 \cdot 10^{-3}}$ $\pm 1.387 \cdot 10^{-4}$

serving the geometry of the data in the synthetic dataset as well as the more noisy and high dimensional dataset.

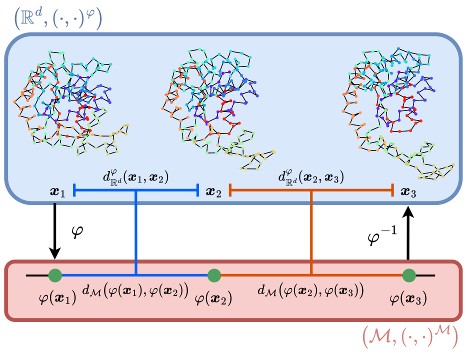
$(\mathbb{R}^d, (\cdot,\cdot)^\varphi)$
$d^\varphi_{\mathbb{R}^d}(\boldsymbol{x}_1, \boldsymbol{x}_2)$
$d^\varphi_{\mathbb{R}^d}(\boldsymbol{x}_2, \boldsymbol{x}_3)$
$\boldsymbol{x}_1$
$\boldsymbol{x}_2$
$\boldsymbol{x}_3$
φ
φ^{-1}
$\varphi(\boldsymbol{x}_1)$
$d_\mathcal{M}(\varphi(\boldsymbol{x}_1), \varphi(\boldsymbol{x}_2))$
$\varphi(\boldsymbol{x}_2)$
$d_\mathcal{M}(\varphi(\boldsymbol{x}_2), \varphi(\boldsymbol{x}_3))$
$\varphi(\boldsymbol{x}_3)$
$(\mathcal{M}, (\cdot,\cdot)^\mathcal{M})$

Figure 3: Isometric learning for AK dataset, coarse-grained protein conformation data. We define a new metric $(\cdot,\cdot)^\varphi$ on the ambient space, $\mathbb{R}^d$ ($d = 214 \times 3$), by learning a diffeomorphism $\varphi : \mathbb{R}^d \to \mathcal{M}$ that preserves a locally Euclidean metric $(\cdot,\cdot)^\mathcal{D}$ on the latent manifold $\mathcal{M} = \mathcal{M}_{d'} \times \mathbb{R}^{d-d'}$ for $d' = 1$.

5.2. Interpolation Experiments

The goal of isometric learning is to learn an interpolatable latent (sub)manifold of the data manifold with closed-form manifold mappings. To evaluate whether interpolation on the latent (sub)manifold accurately reflects interpolation on the data manifold, we conduct an interpolation experiment using the synthetic ARCH dataset, as well as the molecular dynamics datasets of Adenylate Kinase (AK) and I-FABP, see Figure 3 for the example of isometric learning on the AK dataset.

In both cases we choose $\mathcal{M}_{d'} = \mathbb{R}$, see Appendix D for guidance on latent manifold and metric selection. We approximate the metric on the data manifold $(\cdot,\cdot)^\mathcal{D}$ through the length of Isomap's geodesics (Tenenbaum et al., 2000), see Figure 4 for an example. We compare the accuracy of the 100 longest geodesics between points in the test set for multiple (latent) interpolation methods.

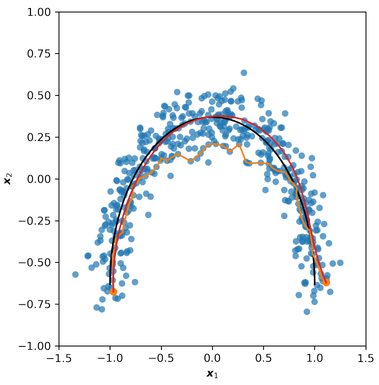

Figure 4: Example of $(\cdot,\cdot)^{\mathcal{M}_{d'}}$-interpolation for ARCH dataset in **red**. In **blue** the dataset $\{\boldsymbol{x}_i\}_{i=1}^n$, **black** the true submanifold $\mathcal{M}_{d'}$, the half circle, and in **orange** the Isomap geodesic between **orange points**.

Result. The $(\cdot,\cdot)^{\mathcal{M}_{d'}}$- and $(\cdot,\cdot)^{\mathcal{M}}$-interpolation achieves superior interpolation accuracy with lower RMSE variablity compared to other models, indicating more robust and reliable interpolation. $(\cdot,\cdot)^{\mathcal{M}_{d'}}$-interpolation specifically demonstrates improvements over other methods in the more stochastic and seemingly higher dimensional AK ($d = 639$) and I-FABP ($d = 642$) datasets. This improvement suggests that compressing the latent representation into a lower-dimensional space reduces the noise while accurately capturing the underlying data manifold. Our findings demonstrate that accurate interpolation of protein dynamics trajectories of AK and I-FABP can be achieved using a single-dimensional latent manifold. This method shows promise for improving protein dynamics simulations.

Table 2: Root mean square error (RMSE) (↓) of the 100 longest isomap geodesics in the test set for 3 different seeds for linear interpolation, $(\cdot,\cdot)^{\mathcal{M}}$-interpolation and $(\cdot,\cdot)^{\mathcal{M}_{d'}}$-interpolation, compared to latent interpolation methods variational autoencoders (VAEs) (Kingma & Welling, 2013), $\beta-$VAEs (Higgins et al., 2017) and GRAE (Duque et al., 2022).

Interpolation	**Latent**	**ARCH**	**Swiss Roll**	**AK**	**I-FABP**
Linear	✗	$0.331_{\pm 0.049}$	$0.573_{\pm 0.018}$	$0.554_{\pm 0.131}$	$0.494_{\pm 0.022}$
VAE	✓	$0.526_{\pm 0.024}$	$0.596_{\pm 0.085}$	$1.235_{\pm 0.477}$	$0.405_{\pm 0.023}$
β-VAE	✓	$0.527_{\pm 0.025}$	$0.640_{\pm 0.066}$	$0.919_{\pm 0.631}$	$0.368_{\pm 0.009}$
GRAE (Isomap)	✓	$0.426_{\pm 0.076}$	$0.568_{\pm 0.024}$	$2.030_{\pm 0.579}$	$0.442_{\pm 0.005}$
GRAE (PHATE)	✓	$\mathbf{0.128}_{\pm 0.052}$	$0.660_{\pm 0.150}$	$1.012_{\pm 0.395}$	$0.474_{\pm 0.040}$
$(\cdot,\cdot)^{\mathcal{M}}$	✓	$\mathbf{0.097}_{\pm 0.030}$	$\mathbf{0.159}_{\pm 0.054}$	$0.296_{\pm 0.058}$	$0.415_{\pm 0.025}$
$(\cdot,\cdot)^{\mathcal{M}_{d'}}$	✓	$\mathbf{0.109}_{\pm 0.026}$	$\mathbf{0.159}_{\pm 0.055}$	$\mathbf{0.219}_{\pm 0.012}$	$\mathbf{0.292}_{\pm 0.006}$

5.3. Generation Experiments

We demonstrate the effectiveness of our proposed method PFM for generation on data manifolds $\mathcal{D}$. We train two PFMs, one using the latent manifold $\mathcal{M}$ and one using the lower dimensional latent submanifold $\mathcal{M}_{d'}$, named PFM and d'-PFM respectively. Additionally, we train a Conditional Flow Matching (CFM) model on the raw data as a comparison. A visual example of the learned generative flows over time for the ARCH dataset can be viewed in Figure 2. To evaluate our generative methods, we use the 1-nearest neighbour (NN) accuracy (Lopez-Paz & Oquab, 2016), which measures how well the generated point clouds match the reference point clouds. Each point cloud is classified by finding its nearest neighbor in the combined set of generated and reference point clouds. The accuracy reflects how similar the generated point clouds are to the reference set, with an accuracy close to 50% indicating successful learning of the target distribution.

Result. Figure 2 we see that the learned isometry to the latent manifold $\mathcal{M}$ acts as a strong manifold prior, capturing the manifold structure at the start of the continous normalizing flows (CNF) trajectory ($t = 0.0$). Additionally, the learned isometry to the latent submanifold $\mathcal{M}_{d'}$ captures the noiseless manifold revealing the underlying manifold used to generate the data. Through this strong (noiseless) manifold prior, we see that both PFM and 1-PFM approximate the distribution on the manifold earlier in the trajectory and better. Table 3 highlights the effectiveness of the 1-PFM model in generative tasks. The 1-PFM model leverages the lower-dimensional isometric latent manifold $\mathcal{M}_{d'}$, significantly reducing the number of parameters required. Training the 1-PFM is significantly faster due to the reduction in parameters and the dimensionality of the training samples. The 1-NN accuracy for 1-PFM approaches the ideal 0.5 across all datasets, indicating that this model better captures the underlying distribution on the data manifold compared to CFM and PFM.

5.4. Designable Latent Manifolds for Novel Protein Engineering

The goal of these experiments is to design a latent manifold that captures biologically relevant properties of protein sequences, enabling the generation of novel proteins with specific characteristics. By leveraging our method's flexibility in defining the metric on the data manifold $(\cdot,\cdot)^{\mathcal{D}}$, we structure the latent space such that it captures protein properties, such as sequence similarity, hydrophobicity, hydrophobic moment, charge, and isoelectric point.

Table 3: Evaluation of generative model performance across dimensionality of (latent) (sub)manifold (↓), number of model parameters, denoted by # pars (↓), and 1-NN accuracy (1-NN→ 0.5). The 1-NN metric measures the generative quality, with values closer to 0.5 indicating better performance.

	ARCH			**Swiss**		
Model	**dim**	**# pars**	**1-NN**	**dim**	**# pars**	**1-NN**
CFM	2	50562	$0.295_{\pm 0.031}$	2	50691	$0.870_{\pm 0.016}$
PFM	2	50562	$0.262_{\pm 0.025}$	2	50691	$0.795_{\pm 0.011}$
1-PFM	**1**	**5697**	$\mathbf{0.487}_{\pm 0.027}$	**1**	**16066**	$\mathbf{0.789}_{\pm 0.019}$
	AK			**I-FABP**		
Model	**dim**	**# pars**	**1-NN**	**dim**	**# pars**	**1-NN**
CFM	642	4682325	$0.386_{\pm 0.000}$	393	1789941	$0.365_{\pm 0.004}$
PFM	642	4682325	$0.356_{\pm 0.097}$	393	1789941	$0.452_{\pm 0.017}$
1-PFM	**1**	**5697**	$\mathbf{0.464}_{\pm 0.022}$	**1**	**5697**	$\mathbf{0.508}_{\pm 0.006}$

To achieve this, we use protein sequences of up to 25 amino acids from the giant repository of AMP activities (GRAMPA) dataset (see Appendix E for details). We construct the following custom metric on the data manifold,

$$d_{\mathcal{D}}(x_i, x_j) = d_{\text{Levenshtein}}(x_i, x_j) + d_{\text{hydrophobicity}}(x_i, x_j) \tag{14}$$

$$+ d_{\text{hydrophobic moment}}(x_i, x_j) + d_{\text{charge}}(x_i, x_j) \tag{15}$$

$$+ d_{\text{isoelectric point}}(x_i, x_j), \tag{16}$$

where the Levenshtein distance measures the number of single-character edits (insertions, deletions, or substitutions) required to transform one sequence into another.

For the remaining four properties—hydrophobicity, hydrophobic moment, charge, and isoelectric point—distances are computed using the difference in property values between sequences. We define the (pseudo)distance as,

$$d_{\text{[property]}}(x_i, x_j) = |f_{\text{property}}(x_i) - f_{\text{property}}(x_j)|. \tag{17}$$

These (pseudo)distances are standardized by dividing by the maximum observed distance in the training data. Since the Levenshtein distance is a proper metric, we ensure that the combined distance $d_{\mathcal{D}}(x_i, x_j)$ remains a valid distance metric. We use the designed metric $(\cdot, \cdot)^{\mathcal{D}}$ on the space of protein sequences with at most 25 amino acids in the GRAMPA dataset to learn an isometry that preserves this metric on the latent manifold $\mathcal{M}$.

To generate protein sequences with specific properties, we sample from a normal distribution around the data points in the latent manifold $\boldsymbol{z} \in \mathcal{M}$. The variability of this sampling process is aligned with the latent variability of the training data $\sigma_{\boldsymbol{z}_{train}}$, scaled by a temperature factor τ, resulting in the following expression,

$$\boldsymbol{z}_i^{(analogue)} = \boldsymbol{z}_i + \tau \mathcal{N}(\boldsymbol{0}, \sigma_{\boldsymbol{z}_{train}} \boldsymbol{I}), \text{ and} \tag{18}$$

$$\boldsymbol{x}_i^{(analogue)} = \varphi_{\boldsymbol{\theta}}^{-1}(\boldsymbol{z}_i) \text{ for } i = 1, \ldots, n_{test}. \tag{19}$$

This sampling methodology is referred to as *analogue generation*, as it does not involve explicitly learning the distribution over the latent manifold. Instead, it generates novel sequences by sampling around existing data points on the latent (sub)manifold of the test set.

To evaluate the effectiveness of the generated sequences, we measure the number of unique sequences that were not present in the original dataset and compare the properties of the generated samples to the properties of their base points. For further specifics on hyperparameters and training procedures, refer to Appendix F.

Results. Designed latent manifolds facilitated the generation of diverse novel protein sequences, demonstrating the effectiveness of our analogue generation methodology. As shown in Table 4, increasing the temperature parameter (τ) directly influenced the diversity of generated sequences. At lower temperatures ($\tau \leq 0.1$), many unique sequences emerged while maintaining similarity to their base points, as indicated by non-significant KS test values. Conversely, higher temperatures ($\tau > 0.1$) resulted in a significant increase in novel sequences, alongside greater divergence from the base sequences. These results suggest that temperature manipulation can strategically balance novelty and similarity, highlighting the effectiveness of isometric learning in structuring the latent space for protein design.

Table 4: Unique protein sequences generated via analogue generation on the latent manifold $\mathcal{M}$ at various temperatures (τ). The table presents the total sequences generated (Total), those already in the dataset (In Data), and the number of novel sequences (Novel). We perform a Kolmogorov-Smirnov test at a 5% significance level to compare novel sequences with their base points. Non-significant Kolmogorov-Smirnov values are shown as X/Y, where X is the number of non-significant properties and Y is the total properties tested.

τ	Total	In Data	Novel	Non-Sign. KS
0.01	689	652	37	5/5
0.05	689	103	586	5/5
0.1	689	35	654	5/5
0.2	689	12	677	2/5
0.5	689	1	688	1/5
1	689	0	689	0/5

6. Conclusion

We introduce Pullback Flow Matching (PFM), a novel framework for simulation-free training of generative models on data manifolds. By leveraging pullback geometry and isometric learning, PFM allows for closed-form mappings on data manifolds while enabling precise interpolation and efficient generation. We demonstrated the effectiveness of PFM through applications in synthetic protein dynamics and small protein generation, showcasing its potential in generating novel, property-specific samples through designable latent spaces. This approach holds significant promise for advancing generative modeling in fields like drug discovery and materials science, where precise and efficient sample generation is critical.

Impact Statement

This paper presents work whose goal is to advance the field of Machine Learning. There are many potential societal consequences of our work, none which we feel must be specifically highlighted here.

Acknowledgements

FK acknowledges support from the ELLIS unit Amsterdam. EB acknowledges that this publication is part of the project SIGN with file number VI.Vidi.233.220 of the research programme Vidi which is (partly) financed by the Dutch Research Council (NWO) under the grant https://doi.org/10.61686/PKQGZ71565. OO acknowledges support from the Swedish Research Council 2020-03107. CBS acknowledges support from the Philip Leverhulme Prize, the Royal Society Wolfson Fellowship, the EPSRC advanced career fellowship EP/V029428/1, the EPSRC programme grant EP/V026259/1, and the EPSRC grants EP/S026045/1 and EP/T003553/1, EP/N014588/1, EP/T017961/1, the Wellcome Innovator Awards 215733/Z/19/Z and 221633/Z/20/Z, the EPSRC funded ProbAI hub EP/Y028783/1, the European Union Horizon 2020 research and innovation programme under the Marie Skodowska-Curie grant agreement REMODEL. This research was also supported by the NIHR Cambridge Biomedical Research Centre (NIHR203312). The views expressed are those of the author(s) and not necessarily those of the NIHR or the Department of Health and Social Care.

References

Arvanitidis, G., Hansen, L. K., and Hauberg, S. Latent Space Oddity: on the Curvature of Deep Generative Models. *arXiv preprint arXiv:1710.11379*, 2017.

Arvanitidis, G., Hauberg, S., and Schölkopf, B. Geometrically Enriched Latent Spaces. *arXiv preprint arXiv:2008.00565*, 2020.

Behrmann, J., Grathwohl, W., Chen, R. T., Duvenaud, D., and Jacobsen, J.-H. Invertible Residual Networks. In *International Conference on Machine Learning*, pp. 573–582. PMLR, 2019.

Bodnar, C., Bruinsma, W. P., Lucic, A., Stanley, M., Brandstetter, J., Garvan, P., Riechert, M., Weyn, J., Dong, H., Vaughan, A., et al. Aurora: A Foundation Model of the Atmosphere. *arXiv preprint arXiv:2405.13063*, 2024.

Chen, R. T. and Lipman, Y. Flow Matching on General Geometries. In *The Twelfth International Conference on Learning Representations*, 2024.

Chen, R. T., Rubanova, Y., Bettencourt, J., and Duvenaud, D. K. Neural Ordinary Differential Equations. *Advances in Neural Information Processing Systems*, 31, 2018.

Cuzzolin, F. Learning Pullback Metrics for Linear Models. In *The 1st International Workshop on Machine Learning for Vision-based Motion Analysis-MLVMA'08*, 2008.

Cvetkovski, A. and Crovella, M. Multidimensional scaling in the Poincaré disk. *arXiv preprint arXiv:1105.5332*, 2011.

Dao, Q., Phung, H., Nguyen, B., and Tran, A. Flow Matching in Latent Space. *arXiv preprint arXiv:2307.08698*, 2023.

Diepeveen, W. Pulling back symmetric Riemannian geometry for data analysis. *arXiv preprint arXiv:2403.06612*, 2024.

Diepeveen, W., Esteve-Yagüe, C., Lellmann, J., Öktem, O., and Schönlieb, C.-B. Riemannian geometry for efficient analysis of protein dynamics data. *Proceedings of the National Academy of Sciences*, 121(33):e2318951121, 2024.

Dsilva, C. J., Talmon, R., Gear, C. W., Coifman, R. R., and Kevrekidis, I. G. Data-Driven Reduction for a Class of Multiscale Fast-Slow Stochastic Dynamical Systems. *SIAM Journal on Applied Dynamical Systems*, 15(3): 1327–1351, 2016.

Duque, A. F., Morin, S., Wolf, G., and Moon, K. R. Geometry Regularized Autoencoders. *IEEE transactions on pattern analysis and machine intelligence*, 45(6):7381–7394, 2022.

Finlay, C., Jacobsen, J.-H., Nurbekyan, L., and Oberman, A. How to Train Your Neural ODE: the World of Jacobian and Kinetic Regularization. In *International Conference on Machine Learning*, pp. 3154–3164. PMLR, 2020.

Ghojogh, B., Ghodsi, A., Karray, F., and Crowley, M. Spectral, Probabilistic, and Deep Metric Learning: Tutorial and Survey. *arXiv preprint arXiv:2201.09267*, 2022.

Gruffaz, S., Poulet, P.-E., Maheux, E., Jedynak, B., and Durrleman, S. Learning Riemannian metric for disease progression modeling. *Advances in Neural Information Processing Systems*, 34:23780–23792, 2021.

Hauberg, S., Freifeld, O., and Black, M. A Geometric take on Metric Learning. *Advances in Neural Information Processing Systems*, 25, 2012.

Hayes, T., Rao, R., Akin, H., Sofroniew, N. J., Oktay, D., Lin, Z., Verkuil, R., Tran, V. Q., Deaton, J., Wiggert, M., et al. Simulating 500 million years of evolution with a language model. *bioRxiv*, pp. 2024–07, 2024.

Higgins, I., Matthey, L., Pal, A., Burgess, C. P., Glorot, X., Botvinick, M. M., Mohamed, S., and Lerchner, A. β-VAE: Learning Basic Visual Concepts with a Constrained Variational Framework. *ICLR (Poster)*, 3, 2017.

Kapusniak, K., Potaptchik, P., Reu, T., Zhang, L., Tong, A., Bronstein, M., Bose, A. J., and Di Giovanni, F. Metric Flow Matching for Smooth Interpolations on the Data Manifold. *arXiv preprint arXiv:2405.14780*, 2024.

Kaya, M. and Bilge, H. Ş. Deep Metric Learning: A Survey. *Symmetry*, 11(9):1066, 2019.

Kingma, D. P. and Welling, M. Auto-Encoding Variational Bayes. *arXiv preprint arXiv:1312.6114*, 2013.

Lebanon, G. Metric Learning for Text Documents. *IEEE Transactions on Pattern Analysis and Machine Intelligence*, 28(4):497–508, 2006.

Lee, J. M. *Introduction to Smooth Manifolds*. Springer, 2012.

Lee, Y., Yoon, S., Son, M., and Park, F. C. Regularized Autoencoders for Isometric Representation Learning. In *International Conference on Learning Representations*, 2022.

Lipman, Y., Chen, R. T., Ben-Hamu, H., Nickel, M., and Le, M. Flow Matching for Generative Modeling. *arXiv preprint arXiv:2210.02747*, 2022.

Little, A., McKenzie, D., and Murphy, J. M. Balancing Geometry and Density: Path Distances on High-Dimensional Data. *SIAM Journal on Mathematics of Data Science*, 4(1):72–99, 2022.

Lopez-Paz, D. and Oquab, M. Revisiting Classifier Two-Sample Tests. *arXiv preprint arXiv:1610.06545*, 2016.

Noé, F. and Clementi, C. Collective variables for the study of long-time kinetics from molecular trajectories: theory and methods. *Current opinion in structural biology*, 43: 141–147, 2017.

Rombach, R., Blattmann, A., Lorenz, D., Esser, P., and Ommer, B. High-Resolution Image Synthesis with Latent Diffusion Models. In *Proceedings of the IEEE/CVF conference on computer vision and pattern recognition*, pp. 10684–10695, 2022.

Sun, X., Liao, D., MacDonald, K., Zhang, Y., Huguet, G., Wolf, G., Adelstein, I., Rudner, T. G., and Krishnaswamy, S. Geometry-Aware Autoencoders for Metric Learning and Generative Modeling on Data Manifolds. In *ICML 2024 Workshop on Geometry-grounded Representation Learning and Generative Modeling*, 2024.

Szymczak, P., Możejko, M., Grzegorzek, T., Jurczak, R., Bauer, M., Neubauer, D., Sikora, K., Michalski, M., Sroka, J., Setny, P., et al. Discovering highly potent antimicrobial peptides with deep generative model HydrAMP. *nature communications*, 14(1):1453, 2023.

Tenenbaum, J. B., Silva, V. d., and Langford, J. C. A Global Geometric Framework for Nonlinear Dimensionality Reduction. *science*, 290(5500):2319–2323, 2000.

Tong, A., Huang, J., Wolf, G., Van Dijk, D., and Krishnaswamy, S. TrajectoryNet: A Dynamic Optimal Transport Network for Modeling Cellular Dynamics. In *International Conference on Machine Learning*, pp. 9526–9536. PMLR, 2020.

Vanderplas, J. and Connolly, A. Reducing the Dimensionality of Data: Locally Linear Embedding of Sloan Galaxy Spectra. *The Astronomical Journal*, 138(5):1365, 2009.

Wessels, D. R., Knigge, D. M., Papa, S., Valperga, R., Vadgama, S., Gavves, E., and Bekkers, E. J. Grounding Continuous Representations in Geometry: Equivariant Neural Fields. *arXiv preprint arXiv:2406.05753*, 2024.

Witten, J. and Witten, Z. Deep learning regression model for antimicrobial peptide design. *BioRxiv*, pp. 692681, 2019.

Younes, L. *Shapes and Diffeomorphisms*, volume 171. Springer, 2010.

Zhu, X., Suk, H.-I., and Shen, D. Matrix-Similarity Based Loss Function and Feature Selection for Alzheimer's Disease Diagnosis. In *Proceedings of the IEEE Conference on Computer Vision and Pattern Recognition*, pp. 3089–3096, 2014.

A. Background

To achieve an interpolatable latent manifold we take a Riemannian geometric perspective. We start by introducing the notation and key concepts of differential and Riemannian geometry, for a formal description see (Lee, 2012). Second, we explain prior work on RAEs (Diepeveen, 2024), a framework for constructing interpolatable latent manifolds. Third, we summarize CFM for generative modeling (Lipman et al., 2022), a scalable way to train generative models in a simulation-free manner. Finally, we discuss how RFM (Chen & Lipman, 2024) generalize CFM to Riemannian manifolds.

A.1. Riemmanian Geometry

A d-dimensional *smooth manifold* $\mathcal{M}$ is a topological space that locally resembles $\mathbb{R}^d$, such that for each point $\boldsymbol{p} \in \mathcal{M}$, there exists a neighborhood U of $\boldsymbol{p}$ and a *homeomorphism* $\psi : U \to \mathbb{R}^d$, called a *chart*. Then the *tangent space* $\mathcal{T}_{\boldsymbol{p}}\mathcal{M}$ at a point $\boldsymbol{p} \in \mathcal{M}$ is a vector space consisting of the tangent vectors at $\boldsymbol{p}$ representing the space of derivations at $\boldsymbol{p}$.

A *Riemannian manifold* $\left(\mathcal{M}, (\cdot,\cdot)^{\mathcal{M}}\right)$ is a smooth manifold $\mathcal{M}$ equipped with a *Riemannian metric* $(\cdot,\cdot)^{\mathcal{M}}$, which is a smoothly varying positive-definite inner product on the tangent space $\mathcal{T}_{\boldsymbol{p}}\mathcal{M}$ at each point $\boldsymbol{p}$. The Riemannian metric $(\cdot,\cdot)^{\mathcal{M}}$ defines the length of tangent vectors and the angle between them, thereby inducing a natural notion of distance on $\mathcal{M}$ based on the lengths of tangent vectors along curves between two points.

The shortest path between two points on $\mathcal{M}$ is called a *geodesic*, which generalizes the concept of straight lines in Euclidean space to curved manifolds. Geodesics on Riemannian manifold are found by minimizing

$$E(\gamma) = \frac{1}{2}\int_0^1 \left(\dot\gamma(t), \dot\gamma(t)\right)_{\gamma(t)} dt, \tag{20}$$

whereas

$$L(\gamma) = \int_0^1 \sqrt{\left(\dot\gamma(t), \dot\gamma(t)\right)_{\gamma(t)}} dt \tag{21}$$

defines the distance between two points on the manifold. The *exponential map*,

$$\exp_{\boldsymbol{p}} : \mathcal{T}_{\boldsymbol{p}}\mathcal{M} \to \mathcal{M}, \tag{22}$$

at $\boldsymbol{p}$ maps a tangent vector $\Xi_{\boldsymbol{p}} \in \mathcal{T}_{\boldsymbol{p}}\mathcal{M}$ to a point on $\mathcal{M}$ reached by traveling along the geodesic starting at $\boldsymbol{p}$ in the direction of $\Xi_{\boldsymbol{p}}$ for unit time. The *logarithmic map*,

$$\log_{\boldsymbol{p}} : \mathcal{M} \to \mathcal{T}_{\boldsymbol{p}}\mathcal{M}, \tag{23}$$

is the inverse of the exponential map, mapping a point $\boldsymbol{q} \in \mathcal{M}$ back to the tangent space $\mathcal{T}_{\boldsymbol{p}}\mathcal{M}$ at $\boldsymbol{p}$.

These names, 'exponential' and 'logarithmic' map, are geometric extensions of familiar calculus concepts. Just as the exponential function maps a number to a point on a curve, the exponential map on a manifold maps a direction and starting point to a location along a geodesic. Similarly, the logarithm in calculus reverses exponentiation, and the logarithmic map on a manifold reverses the exponential map, returning the original direction and distance needed to reach a specified point along the geodesic.

Assume $\left(\mathcal{M}, (\cdot,\cdot)^{\mathcal{M}}\right)$ is a d-dimensional Riemannian manifold and a smooth diffeomorphism $\varphi : \mathbb{R}^d \to \mathcal{M}$, such that $\varphi(\mathbb{R}^d) \subseteq \mathcal{M}$ is geodesically convex, i.e., geodesics are uniquely defined on $\varphi(\mathbb{R}^d)$. We can then define the *pullback metric* as

$$(\Xi_{\mathbf{p}}, \Phi_{\mathbf{p}})^{\varphi}_{\mathbf{p}} := \left(\varphi_*[\Xi_{\mathbf{p}}], \varphi_*[\Phi_{\mathbf{p}}]\right)_{\varphi(\mathbf{p})}, \tag{24}$$

for tangent vectors $\Xi_{\mathbf{p}}$ and $\Phi_{\mathbf{p}}$, where φ_* is the pushforward. These mappings allow us to define all relevant geometric mappings in $\mathbb{R}^d$ in terms of manifold mappings on $\mathcal{M}$, see e.g. Proposition 2.1 of (Diepeveen, 2024):

1. Distances $d^{\varphi}_{\mathbb{R}^d} : \mathbb{R}^d \times \mathbb{R}^d \to \mathbb{R}$ on $\left(\mathbb{R}^d, (\cdot,\cdot)^{\varphi}\right)$ are given by,

$$d^{\varphi}_{\mathbb{R}^d}(\boldsymbol{x_i}, \boldsymbol{x_j}) = d_{\mathcal{M}}\left(\varphi(\boldsymbol{x}_i), \varphi(\boldsymbol{x}_j)\right), \tag{25}$$

2. Length-minimizing geodesics $\gamma^{\varphi}_{\boldsymbol{x}_i,\boldsymbol{x}_j} : [0,1] \to \mathbb{R}^d$ on $\left(\mathbb{R}^d, (\cdot,\cdot)^{\varphi}\right)$ are given by,

$$\gamma^{\varphi}_{\boldsymbol{x}_i,\boldsymbol{x}_j}(t) = \varphi^{-1}\left(\gamma^{\mathcal{M}}_{\varphi(\boldsymbol{x}_i),\varphi(\boldsymbol{x}_j)}(t)\right) \tag{26}$$

3. Logarithmic maps $\log^{\varphi}_{\boldsymbol{x}_i} : \mathbb{R}^d \to \mathcal{T}_{\boldsymbol{x}_i}\mathbb{R}^d$ on $\left(\mathbb{R}^d, (\cdot,\cdot)^{\varphi}\right)$ are given by,

$$\log^{\varphi}_{\boldsymbol{x}_i}(\boldsymbol{x}_j) = \varphi_*^{-1}\left[\log^{\mathcal{M}}_{\varphi(\boldsymbol{x}_i)}\left(\varphi(\boldsymbol{x}_j)\right)\right] \tag{27}$$

4. Exponential maps $\exp^{\varphi}_{\boldsymbol{x}_i} : \mathcal{G}_{\boldsymbol{x}_i} \to \mathbb{R}^d$ for $\mathcal{G}_{\boldsymbol{x}_i} := \log^{\varphi}_{\boldsymbol{x}_i}(\mathbb{R}^d) \subset \mathcal{T}_{\boldsymbol{x}_i}\mathbb{R}^d$ on $\left(\mathbb{R}^d, (\cdot,\cdot)^{\varphi}\right)$ are given by

$$\exp^{\varphi}_{\boldsymbol{x}_i}(\Xi_{\boldsymbol{x}_i}) = \varphi^{-1}\left(\exp^{\mathcal{M}}_{\varphi(\boldsymbol{x}_i)}\left(\varphi_*[\Xi_{\boldsymbol{x}_i}]\right)\right) \tag{28}$$

A visual example of pullback geometry is given in Figure 5. Pullback geometry allows us to remetrize all of space $\mathbb{R}^d$, including the data manifold $\mathcal{D} \subset \mathbb{R}^d$, through the pullback metric. We can use it to define geometric mappings on $\left(\mathbb{R}^d, (\cdot,\cdot)^{\varphi}\right)$, including geodesics (see Equation 26), through geometric mappings on the latent manifold $\mathcal{M}$. Next, we summarize work on Riemannian Auto-Encoders, that leverage pullback geometry to create an interpolatable latent manifold.

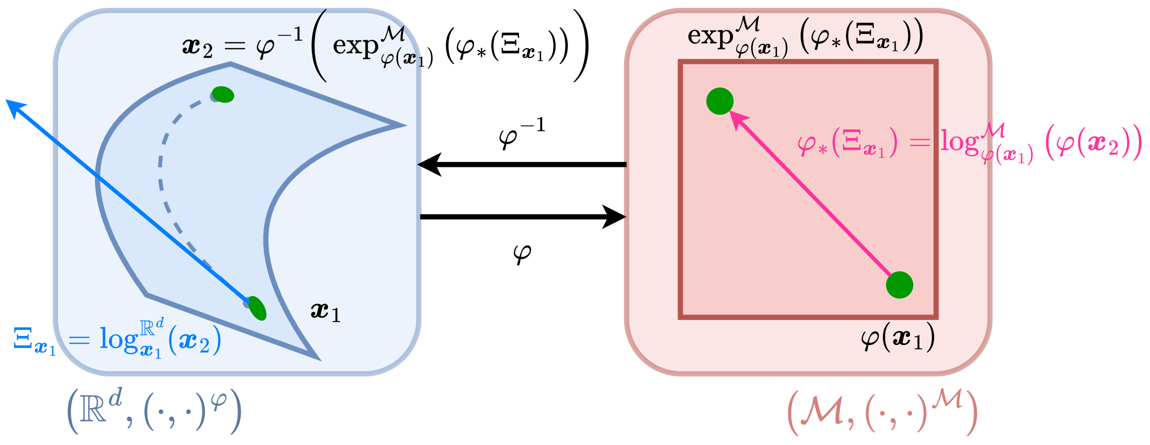
$\boldsymbol{x}_2 = \varphi^{-1}\left(\exp^{\mathcal{M}}_{\varphi(\boldsymbol{x}_1)}\left(\varphi_*(\Xi_{\boldsymbol{x}_1})\right)\right)$
$\exp^{\mathcal{M}}_{\varphi(\boldsymbol{x}_1)}\left(\varphi_*(\Xi_{\boldsymbol{x}_1})\right)$
φ^{-1}
$\varphi_*(\Xi_{\boldsymbol{x}_1}) = \log^{\mathcal{M}}_{\varphi(\boldsymbol{x}_1)}\left(\varphi(\boldsymbol{x}_2)\right)$
φ
$\boldsymbol{x}_1$
$\Xi_{\boldsymbol{x}_1} = \log^{\mathbb{R}^d}_{\boldsymbol{x}_1}(\boldsymbol{x}_2)$
$\varphi(\boldsymbol{x}_1)$
$\left(\mathbb{R}^d, (\cdot,\cdot)^{\varphi}\right)$
$\left(\mathcal{M}, (\cdot,\cdot)^{\mathcal{M}}\right)$

Figure 5: Example of pullback geometry for $\varphi : \mathbb{R}^d \to \mathcal{M}$ with $\mathcal{M} = \mathcal{M}_{d'} \times \mathbb{R}^{d-d'}$ for $\mathcal{M}_{d'} = \mathbb{R}^{d'}$, $d = 3$ and $d' = 2$. Samples $\varphi(\boldsymbol{x}_i)$ are close to elements of $\mathcal{M}_{d'} \times \mathbf{0}^{d-d'}$.

A.2. Riemannian Auto-Encoder

The goal of RAEs is to create a interpolatable latent representation of the data. This is achieved through data-driven (pullback) Riemannian geometry, encoding the data onto a latent manifold with known geometry. The benefit of this, is that interpolation on the data manifold corresponds to interpolation on the latent manifold. Resulting in a more interpretable latent space compared to traditional auto-encoders.

Similar as in (Diepeveen, 2024), we define a RAE as a Riemannian Encoder $\mathrm{RE} : \mathbb{R}^d \to \mathbb{R}^r$ and Riemannian Decoder $\mathrm{RD} : \mathbb{R}^r \to \mathbb{R}^d$,

$$\mathrm{RAE}(\boldsymbol{x}) := (RD \circ RE)(\boldsymbol{x}) \quad s.t., \tag{29}$$

$$\mathrm{RE}(\boldsymbol{x})_k := (\log^{\varphi}_{\boldsymbol{z}}(\boldsymbol{x}), \boldsymbol{v}^k_{\boldsymbol{z}})^{\varphi}_{\boldsymbol{z}} \text{ for } k = 1, \dots r, \tag{30}$$

$$\mathrm{RD}(\boldsymbol{a}) := \exp^{\varphi}_{\boldsymbol{z}}\left(\sum_{k=1}^{r} \boldsymbol{a}_k \boldsymbol{v}^k_{\boldsymbol{z}}\right) \tag{31}$$

where $\boldsymbol{z}$ denotes a base point and $(\cdot,\cdot)^{\varphi}_{\boldsymbol{z}}$ the pullback metric at $\boldsymbol{z}$. Furthermore,

$$\boldsymbol{v}^k_{\boldsymbol{z}} := \sum_{l=1}^{d} \boldsymbol{W}_{lk} \Phi^l_{\boldsymbol{z}}, \tag{32}$$

represents the basis vectors of the latent space in the tangent space $T_{\boldsymbol{z}}\mathbb{R}^d$. Let $\Phi^l_{\boldsymbol{z}} \in T_{\boldsymbol{z}}\mathbb{R}^d$ be an orthonormal basis in the tangent space at $\boldsymbol{z}$ with respect to $(\cdot,\cdot)^{\varphi}_{\boldsymbol{z}}$ and define

$$\boldsymbol{X}_{i,l} = \left(\log^{\varphi}_{\boldsymbol{z}}(\boldsymbol{x}^i), \Phi^l_{\boldsymbol{z}}\right)^{\varphi}_{\boldsymbol{z}} \text{ for } i = 1, \dots, n \text{ and } l = 1, \dots, d. \tag{33}$$

We can compute $\boldsymbol{W}$ through a Singular Value Decomposition (SVD) of $\boldsymbol{X}$.

$$\boldsymbol{X} = \boldsymbol{U}\boldsymbol{\Sigma}\boldsymbol{W}^T, \tag{34}$$

where $U \in \mathbb{R}^{N\times R}$, $\Sigma = \operatorname{diag}(\sigma_1, \ldots, \sigma_R) \in \mathbb{R}^{R\times R}$ with $\sigma_1 \geq \cdots \geq \sigma_R$, $W \in \mathbb{R}^{d\times R}$ and where $R := \operatorname{rank}(\boldsymbol{X})$. The first r columns of $\boldsymbol{W}$, corresponding to the largest singular values, are selected to form the matrix $\boldsymbol{W} \in \mathbb{R}^{d\times r}$. This parameter r allows one to set the dimensionality of the latent representation of the RAE, if $r = d$ then the RAE reduces to $\operatorname{RAE}(\boldsymbol{x}) = \exp^{\varphi}_{\boldsymbol{z}}\left(\log^{\varphi}_{\boldsymbol{z}}(\boldsymbol{x})\right)$.

To learn a RAE, one needs to first construct a diffeomorphism and define an objective function. In (Diepeveen, 2024) diffeomorphisms are constructed by,

$$\varphi := [\psi^{-1}, \boldsymbol{I}_{d-d'}] \circ \phi \circ \boldsymbol{O} \circ T_{\boldsymbol{z}}, \tag{35}$$

where $\psi : U \to \mathbb{R}^{d'}$ is a chart on a (geodesically convex) subset $U \subset \mathcal{M}^{d'}$ of a d'-dimensional Riemannian manifold $(\mathcal{M}^{d'}, (\cdot,\cdot)_{\mathcal{M}'_d})$, $\phi : \mathbb{R}^d \to \mathbb{R}^d$ is a real-valued diffeomorphism, $\boldsymbol{O} \in \mathbb{O}(d)$ is an orthogonal matrix, and $T_{\boldsymbol{z}} : \mathbb{R}^d \to \mathbb{R}^d$ is given by $T_{\boldsymbol{z}}(\boldsymbol{x}) = \boldsymbol{x} - \boldsymbol{z}$. The learnable diffeomorphism $\varphi := \varphi_{\boldsymbol{\theta}}$ is constructed through parameterizing $\phi := \phi_{\boldsymbol{\theta}}$ by an invertible residual network (Behrmann et al., 2019).

A.3. Learning Isometries with Riemannian Auto-Encoders

After constructing the diffeomorphism and Riemannian Auto-Encoder, one can learn an isometry by find the parameters $\boldsymbol{\theta}$ of φ_θ in (Diepeveen, 2024) through minimizing the objective,

$$\begin{aligned}
\mathcal{L}(\boldsymbol{\theta}) = {} & \frac{1}{N(N-1)} \sum_{i,j=1, i\neq j}^{N(N-1)} \left(d^{\varphi_{\boldsymbol{\theta}}}_{\mathbb{R}^d}(\boldsymbol{x}_i, \boldsymbol{x}_j) - d_{i,j}\right)^2 && \text{(global isometry loss)} \\
& + \alpha_{\text{sub}} \frac{1}{N} \sum_{i=1}^{N} \left\| \begin{bmatrix} \boldsymbol{I}_{d-d'} & \emptyset \\ \emptyset & \mathbf{0}_{d'} \end{bmatrix} (\phi_{\boldsymbol{\theta}} \circ \boldsymbol{O} \circ T_{\boldsymbol{z}})(\boldsymbol{x}_i) \right\|_1 && \text{(submanifold loss)} \\
& + \alpha_{\text{iso}} \frac{1}{N} \sum_{i=1}^{N} \left\| \left(\left(\boldsymbol{e}^j, \boldsymbol{e}^{j'} \right)^{\varphi_{\boldsymbol{\theta}}}_{\boldsymbol{x}_i} \right)_{j,j'=1}^{d} - \boldsymbol{I}_d \right\|_F^2, && \text{(local isometry loss)}
\end{aligned}$$

where $\|\cdot\|_F$ is the Frobenius norm and $\left(\left(\boldsymbol{e}^j, \boldsymbol{e}^{j'} \right)^{\varphi_{\boldsymbol{\theta}}}_{\boldsymbol{x}_i} \right)_{j,j'=1}^{d}$ denotes a d-dimensional matrix just as $(\boldsymbol{A}_{ij})^d_{i,j=1}$ denotes a matrix.

First, the **global isometry loss** takes global geometry into account, ensuring that the learned distances under the diffeomorphism $\varphi_{\boldsymbol{\theta}}$ approximate the true pairwise distances $d_{i,j}$ between data points. Second, the **submanifold loss** enforces that the data manifold is mapped to $\mathcal{M} = \mathcal{M}^{d'} \times \mathbb{R}^{d-d'}$, preserving the submanifold structure of the data in the latent space. Finally, the **local isometry loss** enforces local isometry, ensuring that small-scale distances and local geometry are preserved under the transformation, which is critical for maintaining the intrinsic geometric properties of the data during dimensionality reduction. For further details on the implementation and theoretical considerations, see (Diepeveen, 2024).

A.4. Conditional Flow Matching

To achieve the goal of accurate generative modeling on data manifolds through isometric learning, we first need to understand generative modeling on Euclidean spaces. We do this through summarizing CFM (Lipman et al., 2022), a commonly used and effective framework for learning CNFs for generative modeling for Euclidean data (Chen et al., 2018). CFM is a method designed to map a simple base distribution to a target data distribution by learning a time-dependent vector field. The fundamental goal of Flow Matching (FM) is to align a target probability path $p_t(\boldsymbol{x})$ with a vector field $u_t(\boldsymbol{x})$, which generates the desired distribution. The FM objective is defined as follows:

$$\mathcal{L}_{\text{FM}}(\boldsymbol{\eta}) = \mathbb{E}_{t,p_t(\boldsymbol{x})}\|v_t(\boldsymbol{x};\boldsymbol{\eta}) - u_t(\boldsymbol{x})\|^2, \tag{36}$$

where $\boldsymbol{\eta}$ represents the learnable parameters of the neural network that parameterizes the vector field $v_t(\boldsymbol{x};\boldsymbol{\eta})$, and $t \sim \mathcal{U}(0,1)$ is uniformly sampled. However, a significant challenge in FM is the intractability of constructing the exact path $p_t(\boldsymbol{x})$ and the corresponding vector field $u_t(\boldsymbol{x})$.

To address this (Lipman et al., 2022) introduce CFM, a more practical approach by constructing the probability path and vector fields in a conditional manner. The CFM objective is then formulated by marginalizing over the data distribution $q(\boldsymbol{x}_1)$ and considering the conditional probability paths:

$$\mathcal{L}_{\text{CFM}}(\boldsymbol{\eta}) = \mathbb{E}_{t,q(\boldsymbol{x}_1),p_t(\boldsymbol{x}|\boldsymbol{x}_1)}\|v_t(\boldsymbol{x};\boldsymbol{\eta}) - u_t(\boldsymbol{x}|\boldsymbol{x}_1)\|^2. \tag{37}$$

A key result, as established in Theorem 2 of (Chen & Lipman, 2024), is that the gradients of the CFM objective with respect to the parameters $\boldsymbol{\eta}$ are identical to those of the original FM objective, i.e.,

$$\nabla_{\boldsymbol{\eta}}\mathcal{L}_{\text{FM}}(\boldsymbol{\eta}) = \nabla_{\boldsymbol{\eta}}\mathcal{L}_{\text{CFM}}(\boldsymbol{\eta}), \tag{38}$$

ensuring that optimizing the CFM objective yields the same result as the original FM objective. This enables effective train of the neural network without needing direct access to the intractable marginal probability paths or vector fields.

Given a sample $\boldsymbol{x}_1$ from the data distribution $q(\boldsymbol{x}_1)$, we define a conditional probability path $p_t(\boldsymbol{x}|\boldsymbol{x}_1)$ [2]. This path starts at $t = 0$ from a simple distribution, typically a standard Gaussian, and approaches a distribution concentrated around $\boldsymbol{x}_1$ as $t \to 1$:

$$p_t(\boldsymbol{x}|\boldsymbol{x}_1) = \mathcal{N}(\boldsymbol{x}|\mu_t(\boldsymbol{x}_1), \sigma_t(\boldsymbol{x}_1)^2\mathbf{I}), \tag{39}$$

where $\mu_t(\boldsymbol{x}_1) : [0,1] \times \mathbb{R}^d \to \mathbb{R}^d$ is the time-dependent mean, and we denote the time-dependent standard deviation as $\sigma_t(\boldsymbol{x}_1) : [0,1] \times \mathbb{R} \to \mathbb{R}_{>0}$. For simplicity, we set $\mu_0(\boldsymbol{x}_1) = \mathbf{0}$ and $\sigma_0(\boldsymbol{x}_1) = 1$, ensuring that all conditional paths start from the same standard Gaussian distribution. At $t = 1$, the path converges to a distribution centered at $\boldsymbol{x}_1$ with a small standard deviation σ_{min}.

The corresponding conditional vector field $u_t(\boldsymbol{x}|\boldsymbol{x}_1)$ can be defined by considering the flow:

$$\chi_t(\boldsymbol{x}) = \sigma_t(\boldsymbol{x}_1)\boldsymbol{x} + \mu_t(\boldsymbol{x}_1), \tag{40}$$

which maps a sample from the standard Gaussian to a sample from $p_t(\boldsymbol{x}|\boldsymbol{x}_1)$. The vector field $u_t(\boldsymbol{x}|\boldsymbol{x}_1)$ that generates this flow, as proven by (Lipman et al., 2022) in Theorem 3, is given by:

$$u_t(\boldsymbol{x}|\boldsymbol{x}_1) = \frac{\sigma_t'(\boldsymbol{x}_1)}{\sigma_t(\boldsymbol{x}_1)}(\boldsymbol{x} - \mu_t(\boldsymbol{x}_1)) + \mu_t'(\boldsymbol{x}_1), \tag{41}$$

where the primes denote derivatives with respect to time to stay consistent with the original papers notation.

In this work, we choose to use the optimal transport (OT) formulation of CFM. Here, the mean $\mu_t(\boldsymbol{x}_1)$ and standard deviation $\sigma_t(\boldsymbol{x}_1)$ are designed to change linearly in time, offering a straightforward interpolation between the base distribution and the

[2] In this work, we use two types of indexing: x_t to denote time indices and x_i for different data points. It should be clear from the context which indexing is being used.

target distribution. Specifically, the mean and standard deviation are defined as:

$$\mu_t(\boldsymbol{x}_1) = t\boldsymbol{x}_1, \quad \sigma_t(\boldsymbol{x}_1) = 1 - (1 - \sigma_{\text{min}})t. \tag{42}$$

This linear path results in a vector field $u_t(\boldsymbol{x}|\boldsymbol{x}_1)$ given by:

$$u_t(\boldsymbol{x}|\boldsymbol{x}_1) = \frac{\boldsymbol{x}_1 - (1 - \sigma_{\text{min}})\boldsymbol{x}}{1 - (1 - \sigma_{\text{min}})t}. \tag{43}$$

The corresponding conditional flow that generates this vector field is:

$$\chi_t(\boldsymbol{x}) = (1 - (1 - \sigma_{\text{min}})t)\boldsymbol{x} + t\boldsymbol{x}_1. \tag{44}$$

This OT path is optimal in the sense that it represents the displacement map between the two Gaussian distributions $p_0(\boldsymbol{x}|\boldsymbol{x}_1)$ and $p_1(\boldsymbol{x}|\boldsymbol{x}_1)$ (Lipman et al., 2022).

The final CFM loss under this OT formulation is derived by substituting the above vector field and flow into the general CFM objective (Equation 37) and reparameterizing $p_t(\boldsymbol{x}|\boldsymbol{x}_1)$ in terms of $\boldsymbol{x}_0$. This yields the following objective function:

$$\mathcal{L}_{\text{CFM}}(\boldsymbol{\eta}) = \mathbb{E}_{t,q(\boldsymbol{x}_1),p(\boldsymbol{x}_0)} \left\| v_t(\chi_t(\boldsymbol{x}_0); \boldsymbol{\eta}) - \frac{\boldsymbol{x}_1 - (1 - \sigma_{\text{min}})\boldsymbol{x}_0}{1 - (1 - \sigma_{\text{min}})t} \right\|^2. \tag{45}$$

This formulation is advantageous because the OT paths ensure that particles move in straight lines and with constant speed, leading to simpler and more efficient regression tasks compared to traditional diffusion-based methods. We use the OT-CFM objective in this work when we refer to CFM.

A.5. Riemannian Flow Matching

The next step toward generation on data manifolds is understanding generation on manifolds with closed form geometric mappings. RFM aims to do exactly this by generalizing CFM to Riemannian manifolds (Chen & Lipman, 2024). Assume a complete, connected and smooth manifold $\mathcal{M}$ endowed with a Riemannian metric $(\cdot,\cdot)^{\mathcal{M}}$. We are given a set of training samples $\boldsymbol{x}_1 \in \mathcal{M}$ from some unknown data distribution $q(\boldsymbol{x}_1)$ on the manifold. Then the goal is to learn a parametric map $\rho : \mathcal{M} \to \mathcal{M}$ that pushes a simple base distribution p to the data distribution q. To achieve RFM (Chen & Lipman, 2024) reparameterize the conditional flow as

$$\boldsymbol{x}_t = \chi_t(\boldsymbol{x}_0|\boldsymbol{x}_1), \tag{46}$$

where $\chi_t(\boldsymbol{x}_0|\boldsymbol{x}_1)$ is the solution to the ordinary differential equation (ODE) defined by a time-dependent conditional vector field $u_t(\boldsymbol{x}|\boldsymbol{x}_1) \in \mathcal{T}_{\boldsymbol{x}}\mathcal{M}$ that is tangent to the manifold $\mathcal{M}$. The initial condition is set as $\chi_0(\boldsymbol{x}_0|\boldsymbol{x}_1) = \boldsymbol{x}_0$.

This formulation leads to the RFM objective, which ensures that the vector field $u_t(\boldsymbol{x}|\boldsymbol{x}_1)$ learned by the model lies entirely within the tangent space of the manifold at each point $\boldsymbol{x}_t \in \mathcal{M}$:

$$\mathcal{L}_{\text{RFM}}(\boldsymbol{\eta}) = \mathbb{E}_{t,q(\boldsymbol{x}_1),p(\boldsymbol{x}_0)}\left(\left\|v_t(\boldsymbol{x}_t;\boldsymbol{\eta}) - u_t(\boldsymbol{x}_t|\boldsymbol{x}_1)\right\|^{\mathcal{M}}_{\mathbf{x}_t}\right)^2, \tag{47}$$

where $\|\cdot\|_{\mathcal{M}}$ is the norm enduced by the Riemannian metric $(\cdot,\cdot)^{\mathcal{M}}$. For manifolds with closed-form geodesic expressions, a simulation-free objective can be formulated using exponential and logarithmic maps. This approach allows models to be trained without numerically simulating particle trajectories, leveraging closed-form geodesics and mappings to directly compute vector fields and transport paths. In this case, $\boldsymbol{x}_t$ can be defined by the geodesic between $\boldsymbol{x}_1$ and $\boldsymbol{x}_0$ and can be explicitly expressed as

$$\boldsymbol{x}_t = \gamma^{\mathcal{M}}_{\boldsymbol{x}_1,\boldsymbol{x}_0}\big(\kappa(t)\big) = \exp^{\mathcal{M}}_{\boldsymbol{x}_1}\big(\kappa(t)\log^{\mathcal{M}}_{\boldsymbol{x}_1}(\boldsymbol{x}_{\mathbf{0}})\big), \tag{48}$$

with monotonically decreasing differentiable function $\kappa(t)$ satisfying $\kappa(0) = 1$ and $\kappa(1) = 0$ acting as a scheduler. Furthermore, the tangent vector field $u_t(\boldsymbol{x}|\boldsymbol{x}_1)$ can be evaluated through,

$$u_t(\boldsymbol{x}|\boldsymbol{x}_1) = \dot{\gamma}^{\mathcal{M}}_{\boldsymbol{x}_1,\boldsymbol{x}_0}\big(\kappa(t)\big) = \frac{d}{dt}\exp^{\mathcal{M}}_{\boldsymbol{x}_1}\big(\kappa(t)\log^{\mathcal{M}}_{\boldsymbol{x}_1}(\boldsymbol{x}_{\mathbf{0}})\big) \tag{49}$$

The objective function is then given by:

$$\mathcal{L}_{\text{RFM}}(\boldsymbol{\eta}) = \mathbb{E}_{t,q(\boldsymbol{x}_1),p(\boldsymbol{x}_0)}\left(\left\|v_t(\gamma^{\mathcal{M}}_{\boldsymbol{x}_0,\boldsymbol{x}_1}\big(\kappa(t)\big);\boldsymbol{\eta}) - \dot{\gamma}^{\mathcal{M}}_{\boldsymbol{x}_0,\boldsymbol{x}_1}\big(\kappa(t)\big)\right\|^{\mathcal{M}}_{\mathbf{p}}\right)^2 \tag{50}$$

Constructing a simulation-free objective for RFM on general geometries presents significant challenges due to the absence of closed-form expressions for essential geometric operations, such as exponential and logarithmic maps, or geodesics. These operations are crucial for defining and efficiently evaluating the objective but are often computationally intensive to approximate without closed-form solutions. For a list of examples of manifolds with closed-form geometric mappings, see the appendix of (Chen & Lipman, 2024).

In the absence of such closed-form solutions, existing methods tackle these difficulties by either learning a metric that constrains the generative trajectory to align with the data support (Kapusniak et al., 2024) or by assuming a metric with easily computable geodesics on the data manifold (Chen & Lipman, 2024). However, learning a metric can be problematic as it may lead to overfitting or fail to capture the true geometry of the data, particularly when the data manifold is complex or poorly understood. On the other hand, assuming a simple metric with computable geodesics can oversimplify the problem, resulting in models that inadequately represent the underlying data structure. To overcome these challenges, we introduce Pullback Flow Matching in section 3.

B. Closed Form Manifold Mappings

In Table 5, we include a table of manifolds and their closed-form geometric mappings from (Chen & Lipman, 2024). These mappings provide explicit expressions for the exponential and logarithmic maps, which construct local coordinate charts. Given a reference point $\boldsymbol{x} \in \mathcal{M}$, the chart ψ is defined as $\psi(\boldsymbol{y}) = \log^{\mathcal{M}}_{\boldsymbol{x}}(\boldsymbol{y})$, mapping points on the manifold to the tangent space at $\boldsymbol{x}$. The inverse chart is the exponential map, $\psi^{-1}(\Xi) = \exp^{\mathcal{M}}_{\boldsymbol{x}}(\Xi)$, ensuring a local diffeomorphism.

Table 5: Riemannian manifolds with closed-form geometric mappings. The table includes exponential maps, logarithm maps, and inner products, the operator $\oplus$ denotes Möbius addition. For any points $\boldsymbol{x}, \boldsymbol{y} \in \mathcal{M}$ and tangent vectors $\Xi, \Phi \in T_{\boldsymbol{x}}\mathcal{M}$, we use the notation $\| \cdot \|^2_{\mathcal{M}} = (\cdot, \cdot)^{\mathcal{M}}$ for the Riemannian metric. This table is adapted from (Chen & Lipman, 2024).

Manifold $\mathcal{M}$	$\exp^{\mathcal{M}}_{\boldsymbol{x}}(\Xi_{\boldsymbol{x}})$	$\log^{\mathcal{M}}_{\boldsymbol{x}}(\boldsymbol{y})$	$(\Xi, \Phi)^{\mathcal{M}}$
N-D sphere $\{\boldsymbol{x} \in \mathbb{R}^{N+1} : \|\boldsymbol{x}\|_2 = 1\}$	$x \cos(\|\Xi_{\boldsymbol{x}}\|_2) + \frac{\Xi_{\boldsymbol{x}}}{\|\Xi_{\boldsymbol{x}}\|_2} \sin(\|\Xi_{\boldsymbol{x}}\|_2)$	$\arccos\big((\boldsymbol{x}, \boldsymbol{y})\big) \frac{P_{\boldsymbol{x}}(\boldsymbol{y}-\boldsymbol{x})}{\|P_{\boldsymbol{x}}(\boldsymbol{y}-\boldsymbol{x})\|_2}$	$(\Xi_{\boldsymbol{x}}, \Phi_{\boldsymbol{x}})^{\mathcal{M}}$
N-D flat tori $[0, 2\pi]^N$	$(\boldsymbol{x} + \Xi_{\boldsymbol{x}}) \ \% \ (2\pi)$	$\arctan 2\big(\sin(\boldsymbol{y} - \boldsymbol{x}), \cos(\boldsymbol{y} - \boldsymbol{x})\big)$	$(\Xi_{\boldsymbol{x}}, \Phi_{\boldsymbol{x}})^{\mathcal{M}}$
N-D Hyperbolic $\{\boldsymbol{x} \in \mathbb{R}^N : \|\boldsymbol{x}\|_2 < 1\}$	$\boldsymbol{x} \oplus \left(\tanh\left(\frac{\|\Xi_{\boldsymbol{x}}\|_2}{1-\|\boldsymbol{x}\|_2^2}\right) \frac{\Xi_{\boldsymbol{x}}}{\|\Xi_{\boldsymbol{x}}\|_2}\right)$	$(1 - \|\boldsymbol{x}\|_2^2) \tanh^{-1}(\|-\boldsymbol{x} \oplus \boldsymbol{y}\|_2) \frac{-\boldsymbol{x} \oplus \boldsymbol{y}}{\|-\boldsymbol{x} \oplus \boldsymbol{y}\|_2}$	$\frac{4}{(1-\|\boldsymbol{x}\|_2^2)^2} (\Xi_{\boldsymbol{x}}, \Phi_{\boldsymbol{x}})^{\mathcal{M}}$
$N \times N$ SPD matrices	$\boldsymbol{X}^{\frac{1}{2}} \exp\{\boldsymbol{X}^{-\frac{1}{2}} \boldsymbol{U} \boldsymbol{X}^{-\frac{1}{2}}\} \boldsymbol{X}^{\frac{1}{2}}$	$\boldsymbol{X}^{\frac{1}{2}} \log\{\boldsymbol{X}^{-\frac{1}{2}} \boldsymbol{Y} \boldsymbol{X}^{-\frac{1}{2}}\} \boldsymbol{X}^{\frac{1}{2}}$	$\mathrm{tr}\left(\boldsymbol{X}^{-1} \Xi_{\boldsymbol{X}} \boldsymbol{X}^{-1} \Phi_{\boldsymbol{X}}\right)$

C. Neural ODEs Parameterize Diffeomorphisms

We can verify that this defines a diffeomorphism by using Theorem C.15 of (Younes, 2010). According to Theorem C.15, for $\phi_{\boldsymbol{\theta}}$ to be a diffeomorphism, the vector field f must satisfy $f \in L^1([0, 1], C^1_{(0)}(\Omega, \mathbb{B}))$, where Ω is the domain of the vector field and $\mathbb{B}$ is a Banach space representing the target space.

In our case, f is composed of smooth and continuously differentiable functions due to the MLP parameterization, ensuring f is also smooth and continuously differentiable. Additionally, we enforce local isometry by regularizing the Jacobian of $f_{\boldsymbol{\theta}}$, which guarantees local regularity of f in the data domain (see **stability regularization**). Thus, f meets the required conditions and $\phi_{\boldsymbol{\theta}}$ defines a proper diffeomorphism.

D. Manifold and Metric Selection

Isometric learning requires three key choices to be made, first one needs to choose the Riemannian metric of the data manifold $(\cdot, \cdot)^{\mathcal{D}}$, second one needs to choose both the latent (sub)manifold and its Riemannian metric $\big(\mathcal{M}_{d'}, (\cdot, \cdot)^{\mathcal{M}_{d'}}\big)$ and finally one needs to choose the dimensionality d'. Technically one also needs to assume a metric on $\mathbb{R}^{d-d'}$, but in this work we assume a Euclidean metric $(\cdot, \cdot)_2$ throughout all our experiments.

There are several options when selecting the metric on the data manifold $(\cdot, \cdot)^{\mathcal{D}}$. One can choose for example a locally euclidean approximation through Isomap (Tenenbaum et al., 2000) or a more noise-robust geodesic approximation (Little et al., 2022). One can also design a metric to create a latent space [3] structured based on properties of the data one cares about, we show how in subsection 5.4. In this work, we focus on using a proper metric and defer the exploration of learning with pseudo-metrics to future research.

When selecting a latent Riemannian (sub)manifold and metric it is crucial to select $\mathcal{M}_{d'}$ such that $\mathcal{M} = \mathcal{M}_{d'} \times \mathbb{R}^{d-d'}$ it is diffeomorphic to the data manifold $\mathcal{D}$. This ensures that the latent space of the RAE can effectively capture the intrinsic structure of the data. The manifold should be chosen based on its ability to accommodate the data's periodicity, curvature, and dimensionality. This alignment is essential for accurately representing the data manifold within the latent space. Unless otherwise stated we assume $\mathcal{M}_{d'} = \mathbb{R}^{d'}$. Additionally, one should select the Riemannian geometry of $\big(\mathcal{M}_{d'}, (\cdot, \cdot)^{\mathcal{M}_{d'}}\big)$ such that geometric mappings can be explicitly defined in closed form. A list of manifolds with closed form geometric mappings can be found in the appendix of (Chen & Lipman, 2024). Unless otherwise states we select $(\cdot, \cdot)^{\mathcal{M}_{d'}} = (\cdot, \cdot)_2$.

Finally, d', the dimensionality of the latent space, is a hyperparameter that could be tuned through iterative testing. Techniques such as Isomap (Tenenbaum et al., 2000) or equivalents on other manifolds such as hyperbolic space (Cvetkovski & Crovella, 2011) can be employed to evaluate various dimensional and Riemannian geometric settings and determine the optimal d' that balances model complexity with the ability to accurately capture the data manifold's structure.

[3] In this text we refer to the latent space as the concept in machine and representation learning, technically its a latent manifold endowed with a Riemannian metric, not a vector space.

E. Data Description

In this work we use several datasets, synthetic, simulated and experimental. Here we describe them in order of appearance in the experiments.

E.1. ARCH Dataset

We create a dataset in the spirit of (Tong et al., 2020). We sample $n = 500$ data points uniform on the line $[-1, 1]$ ($x_i \sim \mathcal{U}(-1, 1)$), wrap this line around the unit half circle and add normally distributed noise with $\sigma = 0.1$, i.e.

$$y_{i,1} = \sin(0.5\pi x_i) + a_{i,1}, \quad y_{i,2} = \cos(0.5\pi x_i) + a_{i,2} \text{ for } a_{i,j} \sim \mathcal{N}(0, 0.1^2). \tag{51}$$

An example of the dataset can be found in Figure 4.

E.2. Adenylate Kinase (AK)

We consider the time-normalized open-to-close transition of AK. This is a dataset from coarse-grained molecular dynamics simulations consisting of $n = 102$ conformations of 214 amino-acids in $3D$, samples of the trajectory can be found in Figure 6.

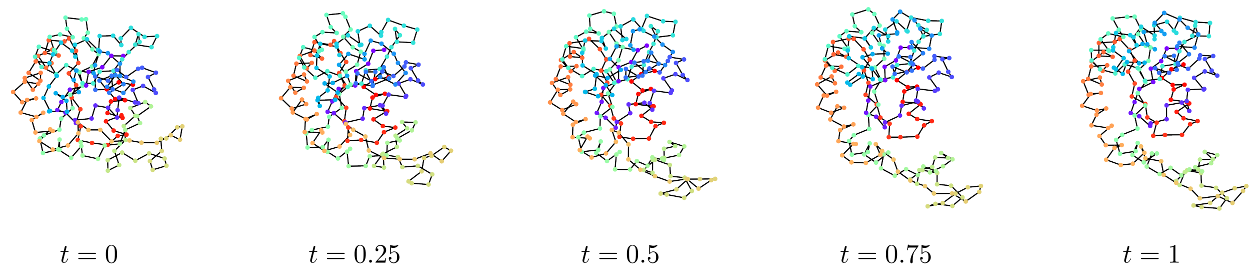

Figure 6: Example of the open-to-close transition of adynalate kinase protein.

E.3. Intestinal Fatty Acid Binding Protein

The second protein dynamics dataset is that of $n = 500$ conformations of I-FABP in water. The datasets comes from simulations in CHARMM of 500 picoseconds (ps) with a 2 femtoseconds (fs) timestep. The data can be found on mdanalysis.org.

E.4. GRAMPA Dataset

The giant repository of AMP activities (GRAMPA) dataset (Witten & Witten, 2019) is a compilation of peptides and their antimicrobial activity against various bacteria, including *E. coli* and *P. aeruginosa*. It includes data on peptide sequences, target bacteria, bacterial strains, and minimal inhibitory concentration (MIC) values, with additional columns providing details on sequence modifications and data sources. The dataset was created to support deep learning models aimed at predicting the antimicrobial effectiveness of peptides. The dataset is available here. In our experiments we follow the preprocessing pipeline from (Szymczak et al., 2023) and use only the sequence data and the corresponding MIC scores. After preprocessing we are left with $n = 3444$ sequences of maximum 25 amino-acids with tested antimicrobial activity against E. coli.

F. Training Procedure

We explain the training procedure and hyperparameter settings for each of the experiments in section 5 in further detail for reproducibility. In all experiments the datasets where split into train and test sets. We apply early stopping and present the model with the lowest average loss on the test data.

F.1. Ablation Study

For details of hyperparameter settings for the ablation study see Table 6.

Table 6: Hyperparameter settings for ablation study of RAE on the ARCH, AK and I-FABP datasets.

Hyperparameter	**ARCH**	**AK**	**I-FABP**
Epochs	1000	1000	1000
Learning Rate	0.0001	0.0001	0.0001
Optimizer	`Adam`	`Adam`	`Adam`
Train/Test Split	$0.8/0.2$	$0.8/0.2$	$0.8/0.2$
n_{steps}	10	10	10
Seed	0	0	0
Number of Layers	5	5	5
α_1	1.0	1.0	1.0
α_2	$[0.0, 1.0]$	$[0.0, 5.0]$	$[0.0, 5.0]$
α_3	1.0	1.0	1.0
α_4	$[0.0, 0.01]$	$[0.0, 0.005]$	$[0.0, 0.1]$
d'	1	1	1
Hidden Units	64	$214 \cdot 3 + 1$	$131 \cdot 3 + 1$
Number of Neighbors	5	2	4
Batch Size	64	16	64
Warmup	50	400	200

Specific hyperparameters worth mentioning are n_{steps} which is the number of Runge-Kutta steps we use in our Neural ODE, *Number of Layers* is the number of layers of the MLP with swish activation function for the vector field of the Neural ODE. The *Number of Neighbors* is the hyperparameter used to calculate the shortest paths over the nearest neighbors graph for the Isomap geodesics in `sklearn` and the *Warmup* is the number of epochs we train with $\alpha_1, \alpha_2 = 0$ to first learn a lower dimensional representation.

F.2. Interpolation Experiments

For details of hyperparameter settings for the interpolation experiments of $(\cdot,\cdot)^{\mathcal{M}}$- and $(\cdot,\cdot)^{\mathcal{M}_{d'}}$-interpolation see Table 7 and for the (β-)VAEs see Table 8.

Table 7: Hyperparameter settings for interpolation experiments for $(\cdot,\cdot)^{\mathcal{M}}$- and $(\cdot,\cdot)^{\mathcal{M}_{d'}}$-interpolation on the ARCH, AK and I-FABP datasets.

Hyperparameters	**ARCH**	**AK**	**I-FABP**	
Epochs	1000	1000	1000	
Learning Rate	0.0001	0.0001	0.0001	
Optimizer	`Adam`	`Adam`	`Adam`	
Train/Test Split	$0.8/0.2$	$0.8/0.2$	$0.8/0.2$	
n_{steps}	10	10	10	
Seed	0	0	0	
Number of Layers	5	5	5	
α_1	1.0	1.0	1.0	
α_2	5.0	5.0	5.0	
α_3	1.0	1.0	1.0	
α_4	0.001	0.005	0.1	
d'	1	1	1	5
Hidden Units	64	$214 \cdot 3 + 1$	$131 \cdot 3 + 1$	
Number of Neighbors	5	2	4	
Batch Size	64	16	64	
Warmup	50	400	200	
$n_{parameters}$	17282	2486480	934961	

Table 8: Hyperparameter settings for interpolation experiments for (β-)VAE on the ARCH dataset. VAEs have $\beta = 1.0$, β-VAEs have $\beta = 10.0$.

Hyperparameters	**ARCH**	**AK**	**I-FABP**
Epochs	1000	1000	1000
Learning Rate	0.0001	0.0001	0.0001
Optimizer	`Adam`	`Adam`	`Adam`
Train/Test Split	$0.8/0.2$	$0.8/0.2$	$0.8/0.2$
Seed	0	0	0
Number of Encoder Layers	5	5	5
Number of Decoder Layers	5	5	5
Hidden Units	64	$214 \cdot 3 + 1$	$131 \cdot 3 + 1$
Beta	$[1.0, 10.0]$	$[1.0, 10.0]$	$[1.0, 10.0]$
d'	1	1	1
Batch Size	64	16	64
$n_{parameters}$	34184	4555655	1712324

F.3. Generation Experiments

Table 9: Hyperparameter settings for CFM, PFM and d'-PFM for generation experiments. The same isometry $\varphi_{\boldsymbol{\theta}}$ of the interpolation experiments is used for the PFM and d'-PFM.

		ARCH			**I-FABP**	
Hyperparameter	CFM	PFM	d'-PFM	CFM	PFM	d'-PFM
Epochs	5000	5000	5000	5000	5000	5000
Learning Rate	0.0005	0.0005	0.0005	0.001	0.001	0.0005
Scheduler	`Cosine`	`Cosine`	`Cosine`	`Cosine`	`Cosine`	`Cosine`
Minimum Learning Rate	$5.0 \cdot 10^{-6}$	$5.0 \cdot 10^{-6}$	$5.0 \cdot 10^{-6}$	$1.0 \cdot 10^{-5}$	$1.0 \cdot 10^{-5}$	$5.0 \cdot 10^{-6}$
Train/Test Split	$0.8/0.2$	$0.8/0.2$	$0.8/0.2$	$0.8/0.2$	$0.8/0.2$	$0.8/0.2$
Seed	0	0	0	0	0	0
Number of Layers	10	10	10	10	10	10
Hidden Units	64	64	16	$131 \cdot 3 + 1$	$131 \cdot 3 + 1$	$131 \cdot 3 + 1$
Batch Size	64	64	64	64	64	64
$n_{\text{simulation steps}}$	10	10	10	10	10	10

F.4. Designable Latent Manifolds for Novel Protein Engineering

In Table 10 one can find the settings for training the isometry on the GRAMPA dataset for the protein sequence design experiments. Specific hyperparameter worth mentioning is the embedding dimensions, we use an embedding layer from the `Flax` library to embed the discrete sequences into a continuous space and use a sign-cosine positional embedding, to embed the location in the sequence of the amino acids in the data.

Table 10: Hyperparameter settings for protein design experiments of the RAEs on the GRAMPA dataset.

Hyperparameters	**Setting**
Epochs	1000
Learning Rate	0.0001
Optimizer	`Adam`
Train/Test Split	$0.8/0.2$
n_{steps}	10
Seed	0
Number of Layers	5
Embedding dimension	8
α_1	5.0
α_2	5.0
α_3	5.0
α_4	0.05
d'	128
Hidden Units	512
Batch Size	128
Warmup	100